Marine Structures 109 (2026) 104089

Contents lists available at ScienceDirect

Marine Structures

journal homepage: www.elsevier.com/locate/marstruc

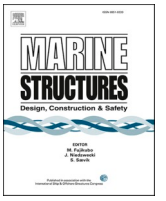

Research Paper

High-fidelity simulation of a novel rope-mesh structure for a floating photovoltaic array in waves

Aditya Nair *, Chenhao Mi, Patrick G Verdin, Luofeng Huang

Faculty of Engineering and Applied Sciences, Cranfield University, Cranfield, MK43 0AL, United Kingdom

ARTICLE INFO

Keywords:
Floating solar farms
Hydrodynamics
Computational Fluid Dynamics
OpenFOAM

ABSTRACT

Floating photovoltaic (FPV) systems offer a promising route for expanding solar generation in coastal and offshore water bodies. However, wave-induced motion, mooring loads, and inter-module forces govern their viability. Excessive motion reduces energy yield, amplifies connector and mooring tensions, and threatens long-term reliability, making accurate hydrodynamic prediction essential for design. Most current CFD studies focus on single-row floaters, typically barge or catamaran-type platforms connected by rigid or hinged connections, leaving the behaviour of multi-row FPVs with compliant inter-module connections largely unexplored. This study develops and validates a high-fidelity CFD framework for rope-mesh FPV arrays, implementing a novel in-memory spring-connector formulation within OpenFOAM's rigidBodyMotion framework to represent compliant, tensioned rope connections. The approach is validated against wave tank experiments for both single-module and 2×2 array configurations. Validation demonstrates excellent accuracy, with heave and pitch RAO errors within 5–13% across wavelengths. The framework successfully captures multi-body interaction effects, including wave-field shielding that reduces aft-row response by upto 10%. Direct comparison demonstrates that conventional rigid joints underpredict pitch by over 20% and overestimate heave by 18%, while the spring connector maintains errors within 5–13%, confirming the necessity of force-based compliant coupling for accurate rope-mesh FPV prediction. Connector force analysis reveals that streamwise connectors experience forces 3–5 times larger than transverse connectors, with peak forces occurring at $\lambda/L \approx 2.5$–3.5, where phase differences maximise differential motion between rows. These results establish streamwise connections as the critical design drivers for rope-mesh FPV systems under head-sea loading.

1. Introduction

1.1. Background

Floating photovoltaics (FPVs) are emerging as an innovative and sustainable solution to the world's growing energy demand, capitalising on underutilised water surfaces. By deploying PV arrays in marine environments, FPVs circumvent land-use conflicts, unlocking opportunities for deployment in urban and rural areas. In addition, the thermal regulation provided by the surrounding water lowers the module operating temperature and enhances the electrical efficiency [1,2]. These advantages have contributed to a

* Corresponding author.
E-mail address: aditya.nair.817@cranfield.ac.uk (A. Nair).

https://doi.org/10.1016/j.marstruc.2026.104089
Received 30 January 2026; Accepted 27 March 2026
Available online 8 April 2026
0951-8339/© 2026 The Authors. Published by Elsevier Ltd. This is an open access article under the CC BY license (http://creativecommons.org/licenses/by/4.0/).

Nomenclature

a	Incident wave amplitude
a_h	Heave motion amplitude
a_p	Pitch motion amplitude
Co	Courant Number
g	Gravitational acceleration
H	Wave height
k	Wavenumber
K	Spring stiffness
L	Characteristic length of FPV
p	Pressure
t	Time
u	Velocity vector
u_c	Compression velocity (VoF)
Δt	Time step
Δx	Local cell size
α	Phase-fraction indicator
η	Free surface elevation
λ	Wavelength
λ/L	Non-dimensional wavelength
μ	Dynamic viscosity
ν	Kinematic viscosity
ρ	Fluid density
ϕ	Phase shift
ω	Angular wave frequency

rapid increase in the installed FPV capacity worldwide.

However, offshore environments pose technical challenges that distinguish them from their inland counterparts. Offshore FPVs are subject to the harsh environment of open oceans, which impacts the hydrodynamic performance and structural integrity of the FPV system [3,4]. These systems must be designed to operate effectively under severe weather conditions, such as storms and cyclones, while the mooring systems must be designed to accommodate the dynamics of FPVs in open-ocean environments [5]. Hence, extensive engineering analyses must be performed to ensure that the developed FPV systems can withstand the harsh open-ocean environment.

A wide variety of FPV configurations have been proposed to address these challenges. Broadly, these can be grouped into pontoon- and superficial-type systems. Pontoon-type FPVs support PV panels on a buoyant platform, which is exposed directly to the wave loading, requiring careful optimisation for seakeeping performance. Superficial-type FPVs position the panels partially within the free surface, making them more susceptible to wave impact and submergence. In both cases, the hydrodynamic behaviour is strongly governed by platform geometry and wave characteristics.

Several CFD studies have investigated the hydrodynamics of FPVs with simplified geometries [6] examined cylindrical pontoon FPVs and reported an inverse relationship between wavelength and heave and pitch response. Additionally, [7] highlighted the importance of the gap effect between twin cylinder FPVs, demonstrating that the local flow interactions can significantly alter motion response. Similarly [8], compared the hydrodynamics of a catamaran-type and semi-submersible pontoon, revealing that the catamaran type has significant seakeeping properties. Study by [9] examined a sun-tracking FPV system coupled with a breakwater, demonstrating reductions in wave height and motion response, while highlighting the need for systematic investigations across a broader range of wave conditions

While single-module investigations provide valuable insight into the fundamental hydrodynamic behaviour of floating photovoltaic (FPV) systems, they are insufficient to fully characterise the response of large-scale FPV arrays. As the number of interconnected modules increases, multi-body hydrodynamic interactions, such as wave shielding, diffraction, and radiation, become dominant and can substantially alter both motion responses and load distributions. Study by [10] demonstrated that, within a row of FPV modules, mooring forces acting on seaward units increase with array length, while central modules experience amplified heave responses due to compressive interactions from neighbouring floaters. Complementary studies have further shown that the ratio of incident wavelength to array length plays a critical role in governing array-scale hydrodynamics, influencing both resonance behaviour and inter-module coupling [11].

The influence of array configuration has been explored through comparative investigations of different hull layouts. Studies by [8,12] reported that increasing the number of can enhance seakeeping performance by distributing wave loads more effectively and [13] compared rectangular and honeycomb arrangements for a six-module FPV array and showing that rectangular configurations exhibit superior motion performance under regular wave conditions. More recently, studies on non-orthogonal layouts, such as star-type FPV arrays, have highlighted the importance of wave directionality, demonstrating that oblique wave incidence can significantly modify array responses and load transfer mechanisms [14].

Table 1
Connector-based studies of FPV's.

Study	Connector Type
[20]	Hinge
[21]	Hinge, fixed
[11]	Hinge
[22]	Rope
[15]	Hinged, rigid, rope, rubber
[17]	Flexible
[23]	Rod type Cardan, Rod type hinged, purely rigid
[18]	Ball joint, Rubber Ring
[24]	Hinge
[19]	Rigid, Cable (elastic)

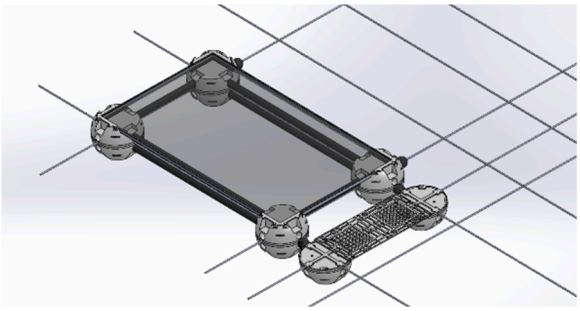

Fig. 1. Rope mesh FPV concept [25].

Inter-module connections play a critical role in determining both the global hydrodynamic response and the structural integrity of FPV arrays. Existing studies have examined rigid, hinged, rubber, and flexible connectors, demonstrating that releasing selected degrees of freedom can significantly reduce transmitted forces. A study by [15,16] showed that rigid connectors experience higher stresses due to constrained motion, while elastic and hinged connections reduce peak loads by allowing relative motion between adjacent units and [17] further reported that connector tension is more sensitive to connector length than diameter, highlighting the importance of connector compliance in load mitigation. More recently, [18,19] demonstrated that elastic connectors outperform rigid systems under energetic wave conditions by dissipating energy through deformation rather than transmitting it directly to the structure. Table 1 summarises prior connector-type investigations, highlighting the predominance of hinge and rigid configurations, as well as the limited attention to tensioned rope-based compliant connections.

1.2. Research gap and scope of this work

Despite the expanding literature on FPV hydrodynamics, a critical limitation persists: existing studies predominantly investigate conventional barge-type and catamaran-based FPVs, often single row, employing rigid, hinged or simplified flexible connections. This leads to several limitations when considering more modular offshore concepts. Load transfer is concentrated to a small number of discrete joints. Rigid and hinged connectors transmit loads through a set of structural links between modules, leading to high stress concentrations and fatigue-sensitive regions in multi-module arrays. These configurations simplify the structural connectivity and tend to suppress relative motion between modules, which limits insights into the behaviour of more compliant modular structures. Furthermore, flexible connections employed in many concepts are realised using cable or rope-like elements that carry only tension. Once such elements enter compression, they do not develop a restoring force and may slacken, allowing large relative motions between modules. In deployment conditions, particularly in nearshore and offshore sites, this slack-taut behaviour is undesirable because it can promote unfavourable relative motion and, in the worst case, contact between the neighbouring FPV units.

The transition to nearshore and offshore FPV deployment demands innovative platform configuration balancing structural simplicity and hydrodynamic performance. As FPV concepts evolve towards larger, modular arrays intended for more energetic nearshore and offshore sites, there is a clear need for validated tools that can resolve how wave parameters and array configurations influence hydrodynamics between modular rows, mooring dynamics and connector loading. To address this need, the present work investigates a rope mesh FPV array [25] as described in Fig. 1, in which FPV platforms are coupled by tensioned connectors arranged in a rectangular mesh configuration. The continuous pre-tensioning in the mesh configuration maintains positive tension across all connectors, preventing slack-taut transitions while permitting controlled relative motion between modules. The hydrodynamic behaviour and resulting connector forces are not well documented, and existing CFD frameworks cannot represent compliant, state-dependent rope connections that maintain tension while permitting controlled relative motion between modules. Understanding how such a system responds to regular waves is essential for defining safe design envelopes and assessing the viability of these systems for large-scale deployment. Within this context, the objective of this study is to develop and validate a coupled experimental and CFD

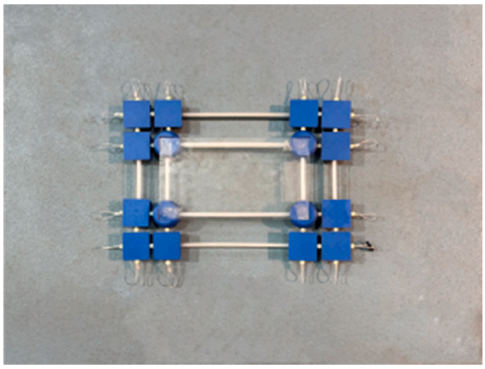

Fig. 2. Single FPV Experimental Model [25].

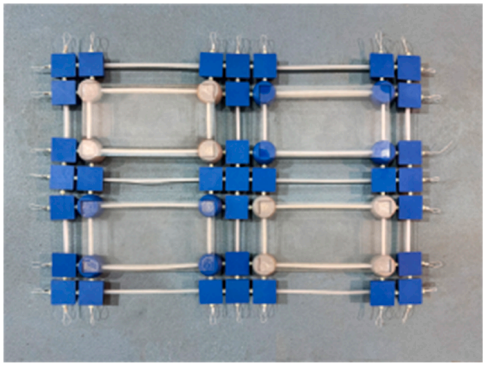

Fig. 3. 2×2 FPV array experimental model [25].

framework capable of predicting motions, mooring loads and connector forces. The principal contributions of this work are threefold: (i) development of a novel in-memory spring-based connector formulation that emulates tension-only rope behaviour; (ii) experimental validation of a coupled CFD-mooring framework for both single-module and 2×2 array configurations; and (iii) systematic characterisation of connector forces under varying wave conditions. The paper is structured as follows: Section 2 details the Experimental Setup, and Section 3 details the computational methodology adopted in this study, including model geometry, domain setup, and solver configuration; Section 4 presents and discusses the results, covering model validation, motion responses, mooring loads, and connection forces; and Section 5 summarises the key findings and outlines design implications for future offshore FPV deployment.

2. Experimental details

To establish a physical benchmark for the numerical simulations proposed in this study, physical wave tank tests were conducted. This section describes the experimental apparatus, the specific rope-mesh geometry, and the instrumentation used to generate the validation data presented in subsequent sections. Fig. 2 depicts the geometry of a single FPV unit used in the experiment. The system consists of a solar panel mounted on top of four spherical buoyancy elements arranged in a rectangular layout. These spherical floaters are interconnected by polyamide rods and nylon ropes, forming a supporting frame for the panel. Additional nylon ropes extend outward to link the structure to adjacent square floaters, creating an overall rectangular structure. Small spherical beads are placed at each connection point. Due to the elastic properties of the nylon ropes and the presence of spherical beads, the joint exhibits a degree of flexibility.

Fig. 3 represents a 2×2 FPV array model employed in the experiment. The 2×2 configuration is constructed by assembling four identical FPV units. These units are interconnected through a network of polyamide ropes, forming a compliant and flexible linkage between neighbouring floaters. The modules also share a set of thirteen square-foot path floaters, which act as common structural nodes across the array. At each interface between the shared footpath floaters and individual FPV units, spherical beads are introduced to regulate rope motion and provide a controlled degree of joint flexibility. The combined effect of the shared floaters and bead-rope interface ensures that the modules remain mechanically connected while preventing direct collisions between adjacent buoyant elements. The combination of shared floaters, polyamide ropes and beads strongly influences the multibody dynamics of the platform. The shared floaters transmit horizontal hydrodynamic forces across the network, causing all four modules to drift forward and backwards largely in a coherent manner when subjected to incident waves. This produces a collective surge response, in which the array behaves as a unified system in the horizontal streamwise direction. In contrast, the compliant connection allows the FPV units to

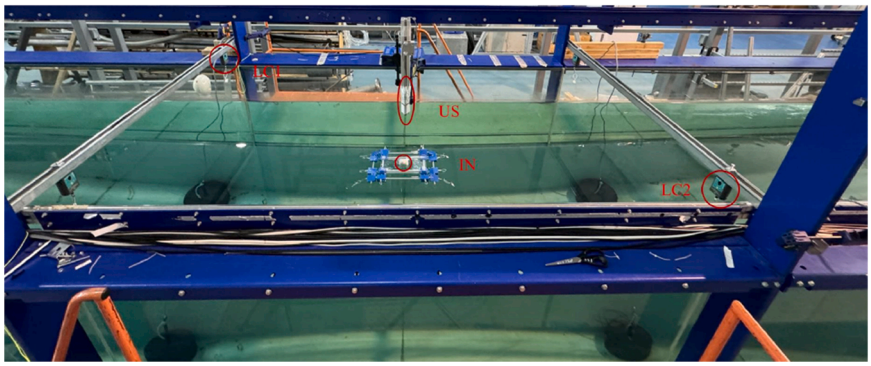

Fig. 4. Experiment setup and instrumentation for FPV tests [25].

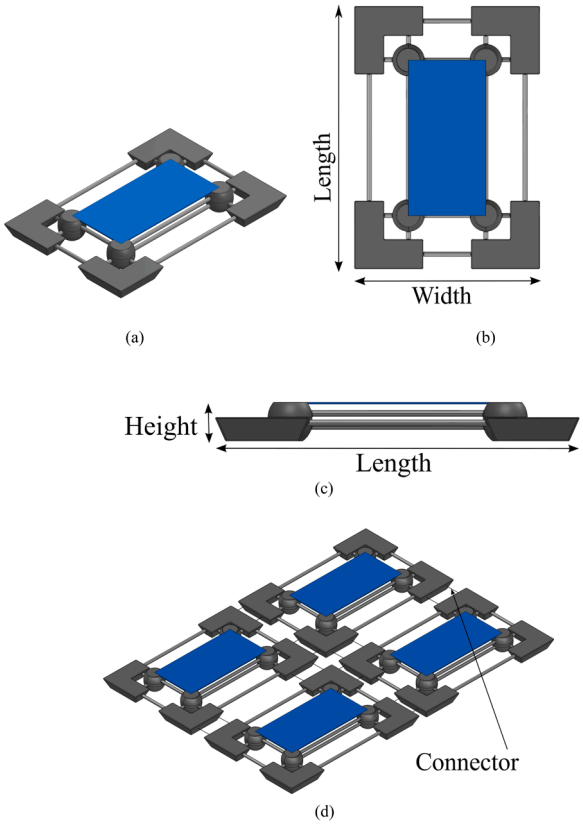

Fig. 5. FPV Geometry (a) Isometric view of single FPV (b) Isometric view of single FPV (c) side view of single FPV (d) Isometric view of 2×2 FPV.

respond individually in heave and pitch direction. As a result, the 2×2 assembly exhibits the characteristic behaviour of rope mesh FPV systems: global synchronisation in surge combined with module-specific heave and pitch motions driven by wave impact.

Fig. 4 describes the setup used in the experiment. The experiment for this validation study was performed in the wave tank at Cranfield University, which measures 30 m in length, 1.5 m in width and 1.5 m in depth. Heave motion was measured using ultrasonic sensors positioned above the platform, and the pitch angle was recorded by inclinometers placed at the centre of the solar panel. The FPV models were anchored using a symmetric mooring system consisting of braided polyethylene fishing lines connected in series with extension springs and load cells. A pulley-like arrangement was used to redirect each mooring line vertically to a frame-mounted load cell positioned away from the test model. This configuration introduced an error of approximately 10% in the measured load due to friction. Despite these minor frictional losses, the experimental data provide a robust dataset for validating the numerical results.

Table 2
Properties of FPV.

Parameter	Value
Length (streamwise, y-axis) (m)	0.390
Width (transverse, x-axis) (m)Width (m)	0.0279
Height (vertical, z-axis) (m)	0.042
Mass (kg)	0.47
Moment of Inertia	
Ixx (pitch, about the transverse axis)	0.0089
Iyy (roll, about the streamwise axis)	0.0032
Izz (yaw, about the vertical axis)	0.0121

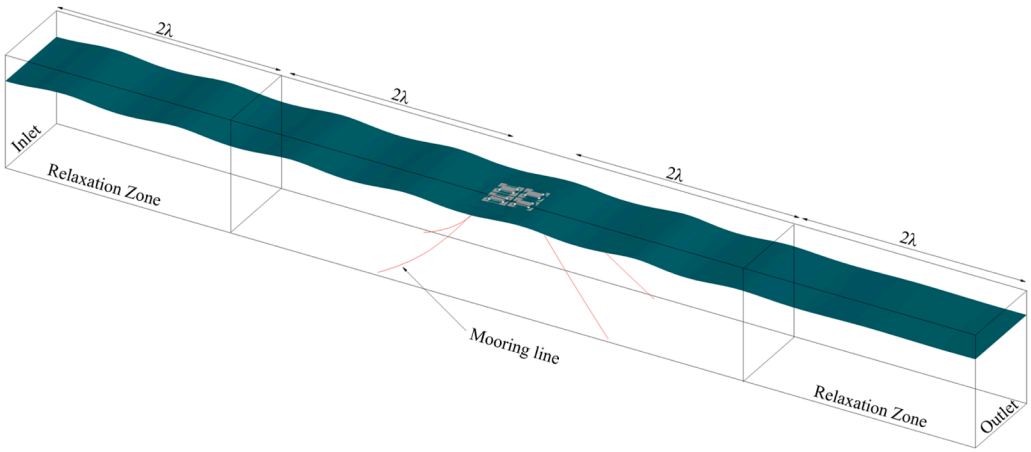

Fig. 6. Isometric view of the computational domain, showing the free surface visualised using the volume-fraction isosurface ($\alpha = 0.5$).

3. Computational methodology

This study employs a Computational Fluid Dynamics (CFD) approach to resolve the complex fluid-structure interactions of the rope-mesh FPV. The numerical model is designed to replicate the experimental setup described in Section 2, ensuring a direct one-to-one validation. The following subsections detail the rigid body geometry, the numerical wave tank domain, the governing equations of the OpenFOAM solver, the rigid joint formulation in OpenFOAM, and the novel in-memory spring connector formulation developed to replicate the rope mesh. Finally, the data processing equation used to obtain the hydrodynamic motion responses and validation results is presented.

3.1. Geometry

Fig. 5(a), (b), (c) depicts a singular FPV module used in the CFD study. All dimensions in the CFD model match those in the experimental model. The coordinate system is defined with the x-axis in the transverse direction (beam/width), y-axis in the streamwise direction (length, positive in the direction of wave propagation), and z-axis vertical (positive upward). The flexibility offered by the rope-bead joint used in the experiment cannot be reproduced directly in the geometry used in CFD. As a result, the CFD representation treats the FPV as a single rigid body, with equivalent mass and inertia properties. This discrepancy in flexibility is expected to introduce differences between the experimental and CFD responses. Table 2 lists the geometric properties of the FPV used in the CFD study.

Fig. 5(d) illustrates the multibody arrangement employed in the CFD study. The four FPV units are retained in a 2×2 arrangement, but the shared footpath floaters are omitted. Explicitly modelling all shared footpath floaters and their local flexibility would substantially increase the number of moving parts and computational cost, while remaining difficult to represent accurately within a rigid-body framework. Instead, each FPV is modelled as an independent rigid body, separated from its neighbours by a gap equal to the width of one square floater. The adopted representation preserves the overall mass and inertia distribution of each FPV and global array layout, while simplifying local connector details. In the CFD study, the inter-module connections provided by the tensioned polyamide ropes in the experiment are represented by spring-based connections acting between rigid FPV bodies, calibrated to reproduce the stiffness and thereby mimic the behaviour of a physical rope mesh. The formulation and implementation of this connection are described in Section 3.4.

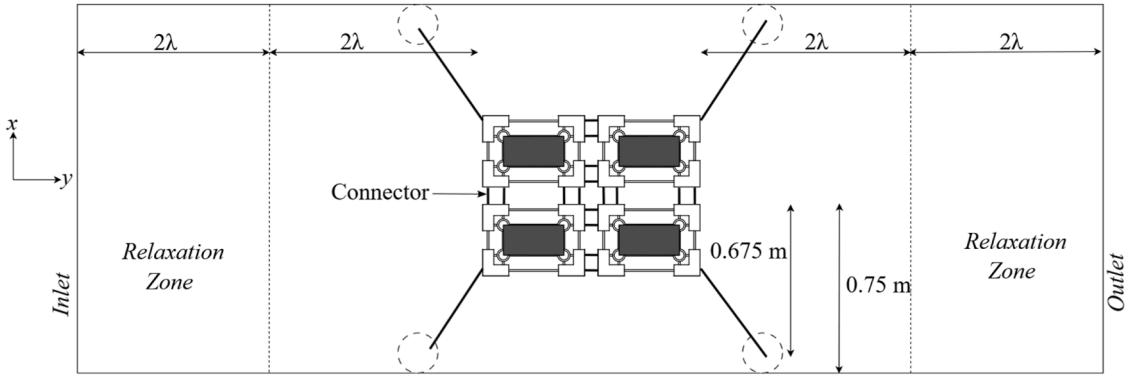

Fig. 7. Top view of the computational domain showing the FPV array layout, relaxation zones, and mooring anchor locations.

Table 3
Boundary conditions.

Field	Inlet	Outlet	Atmosphere	Bed
alpha	zeroGradient	zeroGradient	inletOutlet	zeroGradient
U	zeroGradient	fixedValue	pressure InletOutlet	fixedValue
p	zeroGradient	zeroGradient	totalPressure	zeroGradient

Table 4
Main parameters of the mooring system.

Parameter	Value
Length (m)	2.07
Angle with wave tank (degree)	47
Pretension Force (N)	0.3
Spring Stiffness (N/m)	89.50
Averaged mass per unit length (kg/m)	0.005

3.2. Computational domain

Fig. 6 illustrates the isometric view of the computational domain used in this study. The domain is defined by the Cartesian coordinate system (x, y, z). The free surface is aligned to the x-y plane, and the z-axis is positive upward. The length of the domain is 8 times the target wavelength. The depth and width of the domain are 1.5 m. The FPV is located at 4 wavelengths from the inlet and four wavelengths from the outlet. Fig. 7 illustrates the top view of the CFD domain. In the experiment, weights placed at the edge of the wave tank serve as fixed anchor points. The diameter of the weights is considered while determining the anchor location (marked as a dotted circle). The anchor location is offset by the distance equivalent to the radius of the weights.

Table 3 details the boundary conditions of the computational domain. The bed is modelled as a wall; hence, a zero-velocity (no-slip) boundary condition and zeroGradient conditions are applied to the volume fraction and pressure fields. The atmospheric boundary condition is used such that both the inflow and outflow of mass are permitted. In an open environment, the sidewalls would be treated as either a slip wall or a symmetry wall condition. However, for the purpose of validation, they are modelled as a no-slip wall.

Waves are generated at the inlet boundary condition and propagate along the positive y-direction towards the outlet. The waves2Foam toolbox [26] is employed to generate waves based on Stokes' second-order wave theory. To replicate an open ocean environment, relaxation zones are implemented at the inlet and outlet boundaries. The relaxation zones are employed to mitigate wave reflections that originate from the boundaries, which may disturb the wave generation process.

In addition to the wave generation and absorption framework, the mooring system must be incorporated to replicate the experimental restraint conditions. In this study, the foamMooring package is used to implement the mooring system. FoamMooring [27] is a dedicated mooring library that implements a range of mooring models, including MAP++, MoorDyn (v1 and v2), Moody, for the sixDoFRigidBodyMotion and rigidBodyMotion solvers. The package is compatible for use in overset as well as deform mesh motion, and is compatible with solvers such as interFoam, waveFoam, and olaFlow. As per a study performed by [27,28] MoorDyn mooring restraint offers the user the most flexibility for use and hence was selected for the remainder of this study. Moordyn [29] is a lumped mass model, where the mooring line is discretised starting at the anchor (node 0) and extending to the fairlead (node N+1). Hydrodynamic forces are calculated for the mooring line, but this is for quiescent free surface conditions; wave kinematics is not included in Moordyn.

In the experiments, the mooring system incorporates multiple cable ties to connect to the floater. Furthermore, as per the design of

the near-zero impact system, a pulley arrangement is deployed to place the sensor away from the FPV. Additionally, the experiment includes a spring of given stiffness attached to the end of the mooring line. These features cannot be implemented directly by the standard MoorDyn library. To approximate this arrangement, a simplified model is employed, where the axial stiffness in the MoorDyn input file is calibrated to match the stiffness of the spring. This method represents the elastic characteristic of the mooring line but omits the effects arising from cable-tie geometry and the fishing line spring interface. Consequently, slight discrepancies will arise between the experiment and simulation results. From the experiment, a pre-tension of 0.3 N and at the back for the single body study, and a pre-tension of 0.3 N at the front and 0.5 N at the back is used for the multibody study. Table 4 summarises the parameters of the mooring configuration.

3.3. Description of solver

The present study uses OpenFOAM v2012 (Open-Source Field Operation and Manipulation), an open-source finite volume CFD framework, written in C++. OpenFOAM provides a large set of libraries for discretising and solving partial differential equations on structured and unstructured meshes. The object-oriented architecture enables extension of existing solvers to incorporate additional physics. For this study, the two-phase incompressible solver interFoam is used. The domain employed in this study consists of two fluids, air and water, both of which are assumed to be incompressible in the present study. The governing equations for incompressible laminar fluid flow are given by:-

$$\nabla \cdot u = 0 \tag{1}$$

$$\frac{\partial(\rho u)}{\partial t} + \nabla \cdot (\rho u u) = -\nabla p + \mu \nabla^2 u + \rho g \tag{2}$$

Here, ρ is the density, ν is the kinematic viscosity, p is the pressure, and g is gravity.

The air-water interface is tracked using the Volume of Fluid (VoF) method. A phase-fraction indicator field α represents the local volume fraction of water in each computational cell, defined such that $\alpha = 1$ indicates that the cell is filled with water, $\alpha = 0$ indicates that the cell is filled with air, and $0 \leq \alpha \leq 1$ indicates that the fluid is filled with a mixture of air and water, which is observed in the cells at the air-water interface. Hence, an additional equation must be solved to track the phase. This additional transport equation for phase fraction is given by:-

$$\frac{\partial \alpha}{\partial t} + \nabla \cdot (\alpha u) + \nabla \cdot [\alpha(1-\alpha)u_c] = 0 \tag{3}$$

The third term on the left-hand side introduces artificial compression velocity $\mathbf{u}_c$, which counteracts the numerical diffusion and maintains interface sharpness without requiring excessive mesh refinement [30]. This compression term is active only in the interface region, where $0 < \alpha < 1$. The variation in density and dynamic viscosity in each computational cell can be expressed by the following equation:

$$\rho(\alpha) = \alpha\rho_w + (1-\alpha)\rho_a \tag{4}$$

$$\mu(\alpha) = \alpha\mu_w + (1-\alpha)\mu_a \tag{5}$$

Where subscripts *w* and *a* denote water and air, respectively. This ensures smooth variation of dynamic viscosity and density across the interface.

Pressure velocity coupling is handled using the PIMPLE algorithm, a hybrid scheme combining the PISO (Pressure Implicit with splitting of Operators) and SIMPLE (Semi-Implicit Method for Pressure Linked Equations) algorithms. The algorithm's behaviour is combined with several parameters specified in the fvSolution dictionary. In this study, a single outer loop (nOuterCorrectors = 1) is employed, effectively reducing the algorithm to a PISO type. Within each timestep, the momentum predictor field is activated, followed by two pressure corrector steps (nCorrectors = 2) and one non-orthogonal corrector iteration (nNonOrthogonalCorrectors = 1) to account for mesh non-orthogonality. This combination ensures adequate coupling between the pressure–velocity field, the evolving VoF interface, and the rigid-body motion equations while maintaining stable and efficient solution across all wave conditions.

Spatial discretisation employs second-order accurate schemes to minimise numerical diffusion and dispersion. For the momentum equation, the convective term $\nabla\cdot(\rho\mathbf{uu})$ is discretised using a first-order upwind scheme, while the diffusive term $\mu\nabla 2$ u employs a Gauss-Linear scheme. For the phase fraction, the advection term $\nabla\cdot(\alpha\mathbf{u})$ is discretised using the vanLeer scheme to prevent unphysical results at the interface, while the interface compression term uses Gauss linear discretisation. Time integration is performed using the Crank-Nicolson scheme, with a blending coefficient of 0.3 to enhance numerical stability while maintaining near second-order temporal accuracy. The time step Δt is controlled adaptively based on the Courant number constraints, defined as $Co = |u|\Delta t/\Delta x$, where Δx is the local cell size. Two Courant number limits are enforced: the global Courant number is Co_{max}=0.9 to ensure overall solution stability, and the interface courant number is set to $Co_{\alpha,\ max}$=0.5 to ensure accurate resolution of the free surface.

3.4. Modelling inter-module connections in multi-body FPV arrays

Accurate prediction of multi-body FPV array behaviour requires proper characterisation of inter-module connection mechanics. Two fundamentally different approaches are examined in this study: OpenFOAM's rigid joint implementation based on the

Featherstone articulated body algorithm (Section 3.4.1), and a custom spring-based connector formulation developed to represent compliant rope connections (Section 3.4.2). Both methods are validated against experimental measurements in Section 4, with direct comparison presented in Section 4.3 to establish which approach accurately captures rope-mesh FPV dynamics.

3.4.1. Rigid joint implementation

OpenFOAM's rigidBodyMotion solver utilises a tree-based hierarchical structure combined with the Featherstone articulated body algorithm to simulate coupled motion of interconnected rigid bodies. In this framework, bodies are arranged hierarchically with a single root body serving as the reference frame for the entire system. Each body (except the root) connects to exactly one parent body at a higher hierarchical level, ensuring the connectivity graph remains a tree structure rather than a general graph. This tree structure enables an efficient recursive solution of the multi-body dynamics.

The physics of inter-body connections is defined by two components: the spatial transform X^J, which defines the offset (position and orientation) between bodies, and the joint, which imposes kinematic constraints restricting relative motion to specific degrees of freedom. Mathematically, joints are represented by the motion subspace matrix S, which filters forces and velocities to ensure motion occurs only in permitted directions. For example, a hinge joint allowing rotation only around the X-axis has a motion subspace vector $S = [1, 0, 0, 0, 0, 0]^T$. This matrix determines which degrees of freedom are permitted and which are constrained.

The Featherstone algorithm exploits the tree structure to efficiently solve the system dynamics through three recursive passes. In Pass 1 (kinematic propagation, root to leaves), the spatial velocity of each body i is propagated from its parent:

$$v_i = X_i^J v_{parent} + S_i \dot{q_i} \tag{6}$$

where q_i is the joint velocity. This pass also computes Coriolis and centrifugal accelerations that arise from rotating reference frames. In Pass 2 (inertia aggregation, leaves to root), the algorithm calculates the effective inertia felt by each parent body by accounting for the mechanical freedom of attached children. The articulated body inertia reduction is computed as:

$$I_i^a = I_i^A - I_i^A S_i D_i^{-1} S_i^T I_i^A \tag{7}$$

where $D_i = S_i^T I_i^A S_i$ is the joint-space inertia and D_i^{-1} represents the joint mobility. This step accounts for the fact that a parent does not feel the full inertia of a child in directions where the joint permits free rotation or translation. In Pass 3 (acceleration calculation, root to leaves), the algorithm solves for joint accelerations:

$$\ddot{q}_i = D_i^{-1} \left(u_i - U_i^T a_i' \right) \tag{8}$$

where u_i is the residual force available to drive the joint, and a_i' is the preliminary acceleration assuming the joint is locked. This three-pass approach efficiently propagates kinematic quantities from parent to child while aggregating dynamic quantities from child to parent.

The critical characteristic of this formulation is that joints impose strict kinematic constraints through the motion subspace S. Constraint forces act only perpendicular to the permitted motion:

$$\tau_{constraint} = S^T f_{constraint} \tag{9}$$

In permitted degrees of freedom (where $S \neq 0$), the joint provides zero force-based resistance, and adjacent bodies are kinematically free to move relative to each other without any elastic coupling or restoring force. This approach efficiently handles systems where inter-body connections are genuinely rigid or kinematically constrained. However, it cannot represent connections that exhibit finite stiffness and force-dependent behaviour. For rope-mesh FPV systems, where inter-module connections consist of tensioned ropes with finite axial stiffness, this zero-resistance characteristic in permitted directions makes rigid joints fundamentally unsuitable. The ropes provide elastic coupling that resists relative motion proportionally to displacement, a force-based behaviour that kinematic constraints cannot capture.

3.4.2. Spring-Based connector implementation

The rigid joint formulation described in Section 3.4.1 efficiently handles multi-body systems through kinematic constraints. However, these constraints impose zero force-based resistance in permitted degrees of freedom, making them unsuitable for rope-mesh FPV systems where inter-module connections exhibit stiffness and compliant behaviour. To address this limitation, a custom spring-based connector formulation was developed to represent the elastic coupling characteristics of tensioned rope connections while maintaining computational efficiency within the rigidBodyMotion framework.

To implement this force-based coupling, the software must allow for efficient data exchange between the coupled bodies. While previous implementations, such as [31] achieved this through file-based data exchange; this approach introduced significant I/O overhead and time-lagged force evaluation. In the present work, these limitations are overcome by handling the two dynamic attachment points using direct memory access within the rigidBodyMotion solver. This eliminates time-lag and ensures symmetric force application. At initialisation, the restraint reads and stores parameters, such as the name (index) of the two bodies it links, the local coordinates of the attachment points on each of the bodies, and mechanical properties such as spring stiffness, damping and rest length of the connector. The local attachment points are defined once, and thereafter move rigidly with the corresponding body through the rigidBodyMotion kinematics.

The core of this in-memory operation lies in correctly resolving the position of the dynamic attachment points at every time step.

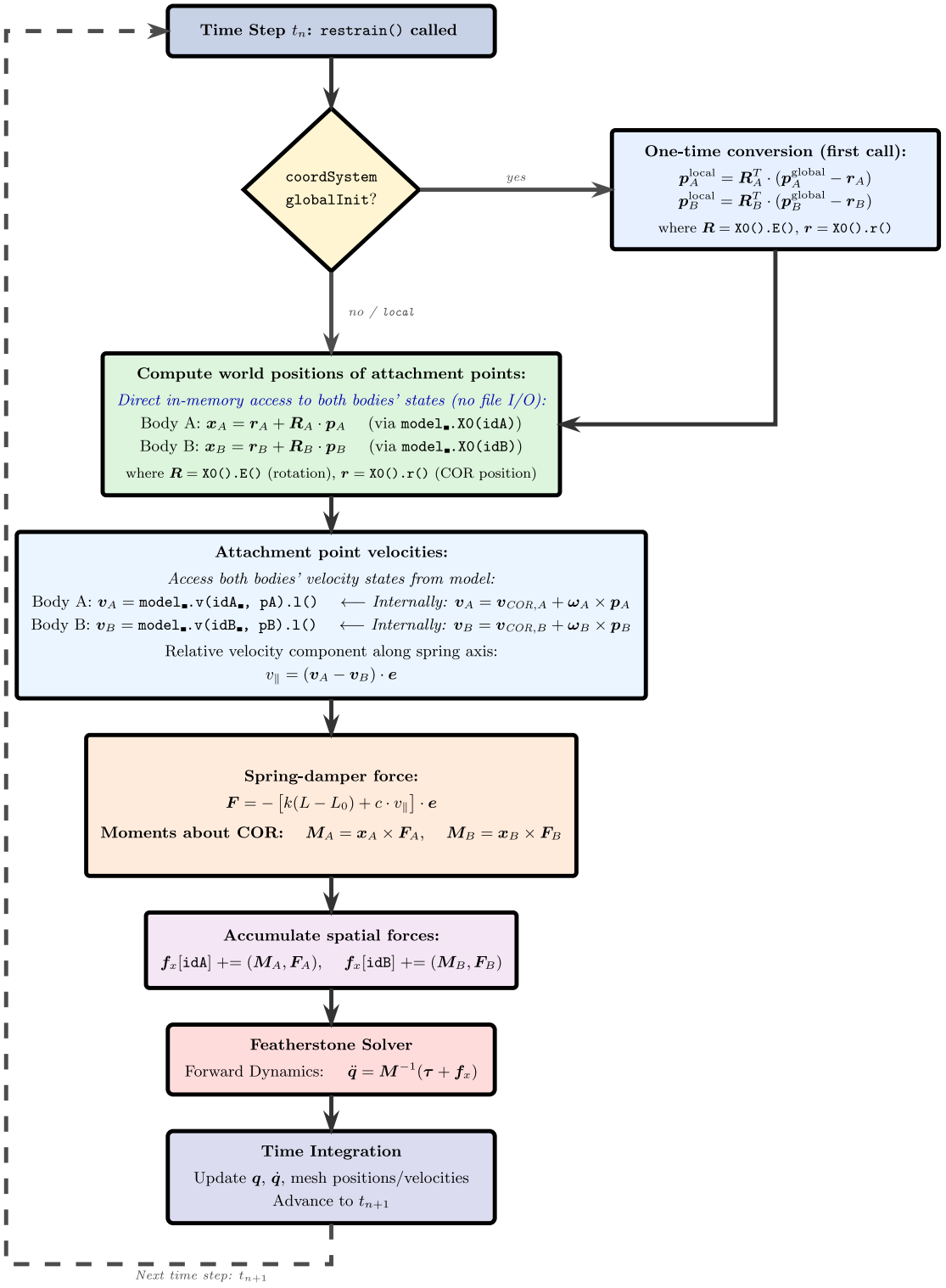

Fig. 8. Connector operation algorithm.

The sequence of operation within one time step is summarised in Fig. 8. At the beginning of the time step t_n, the rigidBodyModel holds the positions and velocities of all bodies. For the connector, the model is first queried for the current kinematics at the two attachment points. The attachment points are defined in local body coordinates as p_A^{local}, p_B^{local} and transformed to the global inertial frame using the

rigid-body transformation:

$$x_A = R_A p_A^{local} + r_A \tag{10}$$

$$x_B = R_B p_B^{local} + r_A \tag{11}$$

where R_A and R_B are the rotation matrices of bodies A and B, and r_A and r_B are their centres of mass in the global frame. This step ensures that the connector always operates on the current configuration and motion state of the two bodies. Once the instantaneous positions are established, the solver must also resolve the velocities to account for damping effects. The velocity at each attachment point is derived by combining the translational velocity of the centre of mass. v_{CoM} with the rotational velocity ω induced by the body's motion:

$$v_A = \omega_A \times (x_A - r_A) + v_{CoM,A} \tag{12}$$

$$v_B = \omega_B \times (x_B - r_B) + v_{CoM,B} \tag{13}$$

Once the attachment point kinematics are known, the connector force is computed. The connector applies elastic and dissipative forces along the instantaneous connector axis. $e = (x_B - x_A)/|x_B - x_A|$. The force acting on body A is given by:

$$F = [K(|x_B - x_A| - L_0) + c(v_B - v_A) \cdot e]e \tag{14}$$

The connector forces generate moments about each body's centre of mass due to the offset of the attachment points:

$$M_A = (x_A - r_A) \times F_A \tag{15}$$

$$M_B = (x_B - r_B) \times F_B \tag{16}$$

Finally, the computed connector loads are aggregated with the hydrodynamic forces from interFoam and the mooring loads from MoorDyn to form the total external load vector. This vector is passed to the Featherstone articulated-body algorithm, which solves the forward dynamics to compute the accelerations and advance the system to the next time step. This coupled framework ensures that the rope-mesh constraints are resolved simultaneously with the fluid-structure interaction.

The proposed connector formulation extends OpenFOAM's rigidBodyMotion framework to enable direct elastic coupling between two dynamic rigid bodies through in-memory force evaluation. The key distinction from the rigid kinematic joints lies in the force-based connection: kinematic joints impose geometric constraints with zero resistance to permitted motions, whereas the spring connector applies restoring forces proportional to displacement and generates moments through spatial offset. This force-based formulation is essential for rope-mesh FPV systems, where inter-module connections exhibit finite stiffness rather than rigid kinematic coupling. The implementation ensures stable load transfer without the time-lag instabilities present in previous file-based implementations. In contrast to previous FPV studies, where connectors are modelled as rigid, hinged, or flexible elements with assumed constitutive behaviour, the present approach resolves time-varying connector forces explicitly within a viscous CFD framework, enabling direct prediction of both array hydrodynamics and inter-module loading in a fully coupled manner. A direct comparison with OpenFOAM's rigid joint is presented in Section 4.4.

3.5. Data processing

Following the completion of each simulation, post-processing is performed to extract hydrodynamic response metrics and connection forces for comparison with experimental measurements. The platform motions are characterised in terms of response amplitude operators (RAO) for heave and pitch, which provide a normalised measure of the structure's dynamic response independent of incident wave amplitude. The RAOs for heave and pitch are calculated according to the following equations:

$$RAO_{Heave} = \frac{a_h}{a}, \quad RAO_{Pitch} = \frac{a_p}{ka} \tag{17}$$

Here, a_h and a_p denote the amplitudes of the heave and pitch motions, respectively. The parameter k represents the wavenumber, and a is the incident wave amplitude. Motion amplitudes are determined by applying Fast Fourier Transform (FFT) to the time histories of heave displacement and pitch angle over the final five wave cycles, extracting the dominant frequency component corresponding to the incident wave frequency. This approach ensures accurate amplitude extraction after the response has converged to a periodic state.

The accuracy of CFD simulations is obtained by comparing simulated results with reference values using the relative error:

$$\text{Relative Error } (\%) = \frac{|CFD - \text{Theoretical}|}{\text{Theoretical}} \times 100 \tag{18}$$

4. Results and discussion

This section presents the validation of the developed CFD framework and its application to analysing rope-mesh FPV arrays under wave loading. Mesh and time-step sensitivity studies are performed to establish appropriate mesh resolution. The hydrodynamic response predictions for both single-module and 2×2 array configurations are compared against experimental measurements across a

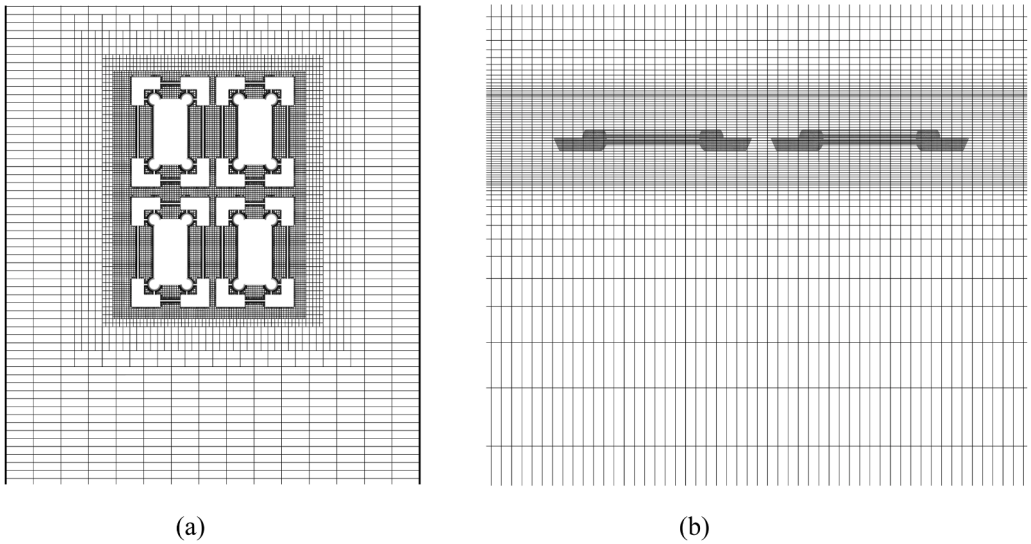

Fig. 9. Image of mesh employed for this study (a) Top View of Mesh (b)Side View of Mesh.

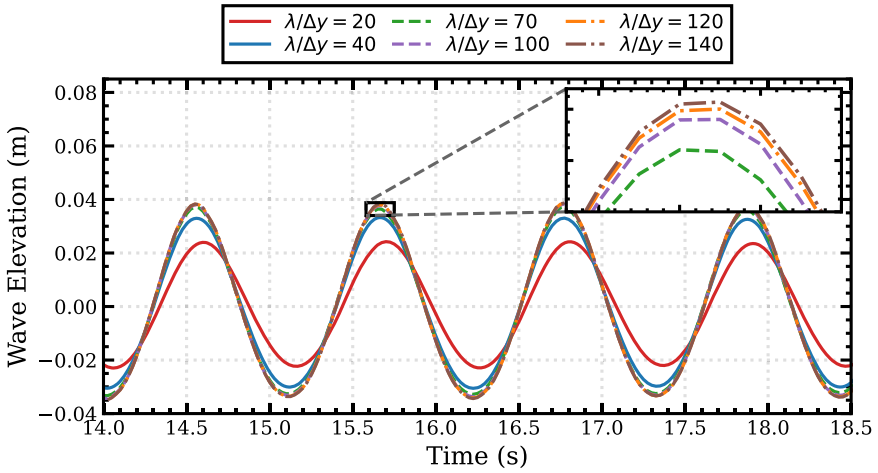

Fig. 10. Free surface elevation time history at varying streamwise mesh resolutions (λ/Δy). The inset shows an enlarged view of the wave crest region demonstrating convergence at higher resolutions.

range of wavelengths and wave heights to assess model accuracy. The section also compares the spring connector formulation with conventional rigid joint approaches to evaluate the importance of force-based coupling for rope-mesh systems. Finally, the validated framework is applied to analyse connector forces under various wave conditions to identify the critical load paths and provide guidance for fatigue assessment in rope-mesh FPV arrays.

4.1. Mesh sensitivity study

Mesh sensitivity analysis is performed to identify the minimum mesh resolution that accurately captures wave propagation, free-surface dynamics, and body motion without high computational cost. A mesh that is too coarse may fail to resolve wave kinematics or introduce numerical diffusion, leading to inaccurate predictions of hydrodynamic forces and motion response. Conversely, excessive refinement increases computational expense without improving accuracy once convergence is achieved. The mesh sensitivity study, therefore, seeks to identify the resolution at which further refinement produces negligible changes in the results.

In OpenFOAM, the initial background mesh is generated via blockMesh, followed by surface mesh generation using snappyHexMesh. Although a preliminary mesh is obtained for wave generation, its resolution is insufficient to capture the surface of the geometry. Hence, the topoSet and refineMesh utility is used to refine the mesh around the body. Fig. 9 depicts the mesh employed in the study. A mesh convergence study is conducted to determine the resolution at which mesh independence is achieved. To verify the quality of wave generation in this study, a mesh independence study is performed to establish the spatial discretisation parameters. In

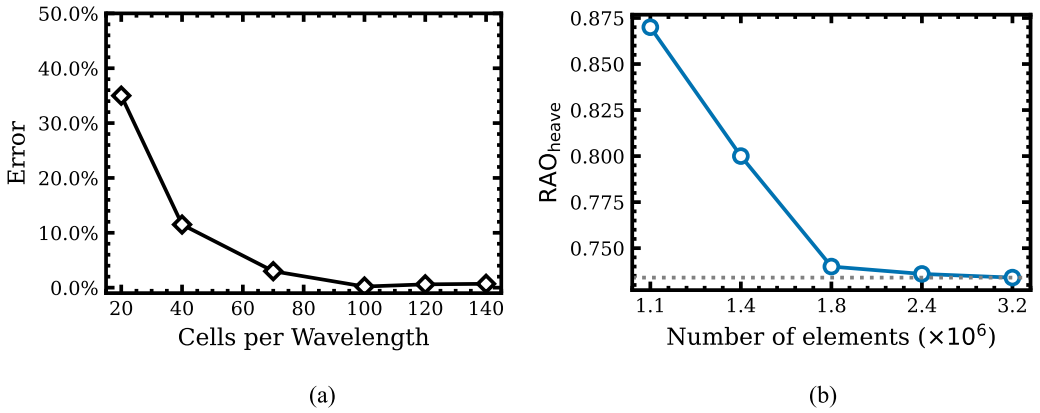

Fig. 11. Mesh Convergence studies (a) Error in free surface at different mesh resolutions (b) RAO value at different mesh levels.

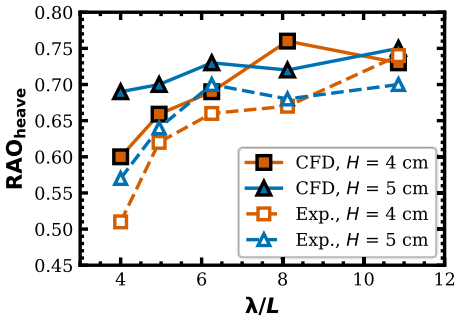

Fig. 12. RAO_{heave} vs non-dimensional wavelength for a single body.

addition, studies from [32–36] are surveyed to draw inspiration for this study. The discretisation parameters are represented in non-dimensional metrics, namely cells per wavelength (λ/Δy) and cells per wave height (H/Δz). In the preliminary study, a vertical resolution of $H/\Delta z = 15$ is fixed, while the streamwise resolution varied through $\lambda/\Delta y = 20, 40, 70, 100, 120, 140$. The mesh sensitivity study is performed for $\lambda = 1.92\ m$ and $a = 4\ cm$. Lower order schemes, such as the Euler method, introduce numerical diffusion which artificially smooths out sharp gradients in the flow. This manifests as a blurring of the air-water interface. To mitigate the error caused by numerical diffusion, we employ a second-order accurate Crank-Nicolson time stepping scheme. This solution is consistent with existing literature [32–36]. This improves sharpness at the interface.

Fig. 10 illustrates the free surface elevation at different $\lambda/\Delta y$ values. While the wave phase is consistently preserved across all cases, the wave crest amplitude exhibits a clear dependence on spatial resolution, with coarser meshes underestimating peak elevations. The enlarged view demonstrates that the solution converges for higher λ/Δy values, indicating that further mesh refinement has a negligible influence on the predicted wave elevation. To further quantify the effect of spatial resolution, Fig. 11(a) shows the relative error as a function of cells per wavelength. The error decreases rapidly with increasing resolution and falls below 5% for $\lambda/\Delta y \geq 70$, reaching a minimum of 0.31% at $\lambda/\Delta y = 100$, after which further refinement yields only marginal improvements, confirming grid convergence of the wave elevation response.

The influence of spatial discretisation was measured through a mesh independence study. Fig. 11(b) illustrates the variation of the heave response amplitude operator with increasing mesh resolution, expressed in terms of the total number of elements. Five distinct mesh densities were selected, comprising 1 M, 1.4 M, 1.8 M, 2.4 M and 3.2 M cells. A pronounced reduction in RAO_{heave} is observed between the coarsest and intermediate meshes, whereas the response asymptotically approaches a constant value for meshes exceeding approximately 1.8 M cells, indicating mesh-independent prediction of the heave response.

4.2. *Validation for a single FPV unit*

With mesh independence established, the framework is applied to simulate the hydrodynamic response of a single FPV module under regular wave conditions. The predicted heave and pitch RAOs are compared against experimental measurements to validate the numerical model's ability to capture wave-structure interaction for an individual floating unit.

Fig. 12 presents the RAO_{heave} for a single body vs non-dimensional wavelength. From the plot, it is evident that the heave increases with increasing wavelength. In the experimental measurements, the variation in heave across wave heights remains within 10%. At $\lambda/L < 5$, the difference across wave heights is more pronounced and diminishes as the wavelength increases. This difference is due to the

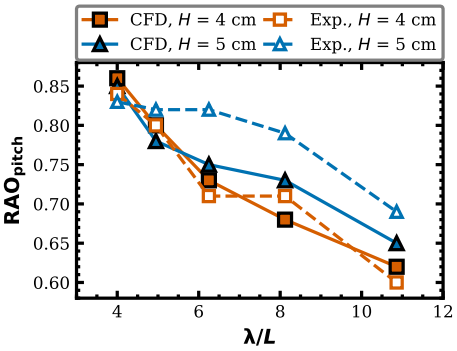

Fig. 13. RAO_{pitch} vs non-dimensional wavelength for a single body.

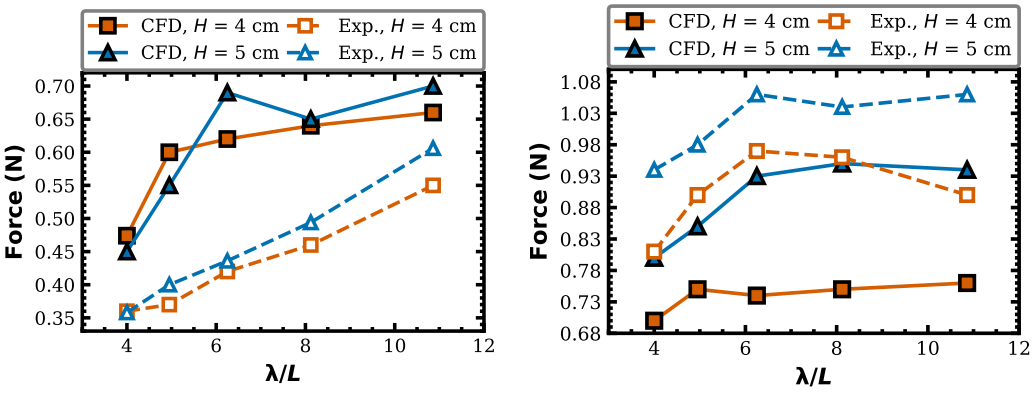

(a) Front mooring force for a single body (b) Rear mooring force for a single body

Fig. 14. Mooring Force for a single body.

flexible nature of the geometry, which dampens part of the amplitude increase at higher steepness, a phenomenon that CFD cannot replicate.

At $\lambda/L = 4.07$, the error between the CFD and experiment is maximum, diminishing progressively as the wavelength grows. This is a consequence of the flexible nature of the geometry used in the experiment, which cannot be replicated in CFD. The nature of flexibility is influential at shorter wavelengths, when the wavelength is closest to the characteristic length of the floater. Overall, the CFD results are in good agreement with the experimental data.

As the non-dimensional wavelength grows, the heave RAO rises from 0.60 at $\lambda/L = 4$ to a peak of 0.76 at $\lambda/L = 8.12$, reducing to 0.73 at $\lambda/L = 11$ for H = 4 cm. A similar increasing trend is observed at H = 5 cm. However, the rate of increase is diminished compared to H = 4 cm. The lowest value of 0.69 is observed at $\lambda/L = 4$, peaking at $\lambda/L = 6$ and then levels with slight fluctuation at $\lambda/L = 8.12$. In the experiment, the heave response of the FPV for H = 5 cm is greater than H = 4 cm at $\lambda/L < 8.12$, which is replicated by the CFD model. At $\lambda/L < 8.12$, the difference in heave response diminishes and at $\lambda/L > 8.12$. Additionally, the deviation between H = 4 cm and H = 5 cm is under 5% across all λ/L values. This behaviour demonstrates that the heave response is insensitive towards the wave height.

Fig. 13 depicts the RAO_{Pitch} plotted against non-dimensional wavelength at two wave heights, H = 4 cm and H = 5 cm. The error at $\lambda/L = 4$ is 3%, which grows to 9% at $\lambda/L = 11$. This behaviour is attributed to the increased twist experienced by the FPV at longer wavelengths in the experiment. Overall, the error in pitch lies within 10% for all values, indicating a good agreement with the experiment. Both the experiment and CFD show the same trend, as the wavelength grows, the RAO_{Pitch} value falls from 0.85 at $\lambda/L = 4$ to 0.62 at $\lambda/L = 11$. Increasing wavelength is accompanied by a decrease in wave steepness; the hydrodynamic moment driving the pitching motion also decreases. Short, steep waves produce strong pitching moments, whereas long, gentle waves lift the front and aft almost in unison, yielding a smaller net pitching.

Similarly, we identify the following trend: the pitch value increases with increasing wave height. This is because the increase in wave height increases the wave steepness, increasing the pitching moment and consequently, shifting the entire RAO_{Pitch} curve upwards. Unlike RAO_{Heave}, the RAO_{Pitch} values for different wave heights lie in proximity. The maximum deviation between the two wave heights is under 5%, indicating a weak sensitivity to wave height. Moreover, the error between the CFD and experiment increases with the increasing wavelength.

Fig. 14 depicts the mooring force of the front and aft mooring lines as the incident wavelength is varied. A comparison of the CFD

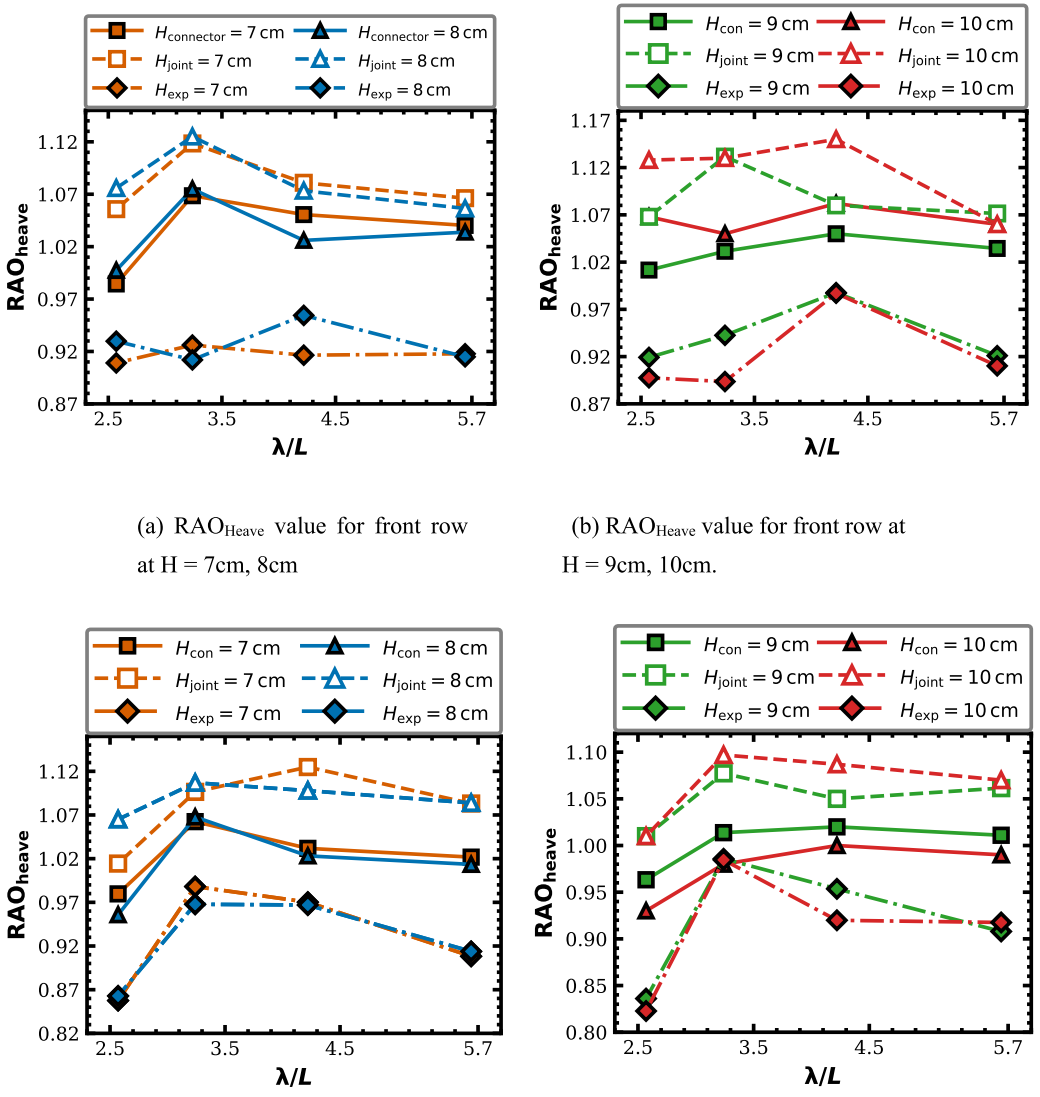

(a) RAO_{Heave} value for front row at H = 7cm, 8cm

(b) RAO_{Heave} value for front row at H = 9cm, 10cm.

(c) RAO_{Heave} value for back row at H = 7cm, 8cm

(d) RAO_{Heave} value for back row at H = 9cm, 10cm

Fig. 15. RAO_{Heave} value for 2 × 2 array of floaters.

and experimental results in Fig. 14(a) reveals that the CFD model overestimates the mooring force by 20–30%. This bias originates from the rigid body geometry. In the CFD geometry, the rigid body is always engaged with the mooring line, transmitting every increment of FPV motion as a load. Within the experiment, the mooring lines are attached to flexible footpath floaters. Load shedding occurs through the bending of the footpath floaters, the frictional effects at the anchor location, and unequal mooring line length. Furthermore, the presence of cable ties cannot be replicated. All these factors contribute to the disparity between the CFD and the experiment.

Despite the errors in magnitude, CFD and experiment exhibit similar trends in wave height and wavelength. For wave heights $H = 4$ *cm* and $H = 5$ *cm*, the mooring force rises linearly by 0.25 N and 0.35 N, respectively. For H = 4 cm, we primarily identify two regimes: A sharp increase in mooring force at $\lambda/L \langle 5$, followed by a gradual rise at $\lambda/L \rangle 5$. For H = 5 cm, a sharp increase is found at $\lambda/L \langle 6.2$, followed by a dip between $6.2 < \lambda/L < 8.2$, after which the mooring force climbs again for $\lambda/L \rangle 8.2$.

Both the experiment and CFD results show that the mooring force increases as the wavelength increases. Longer waves induce larger surge motions and, hence, greater mooring forces. The discrepancy between the CFD and experimental results arises from differences in the physical setup, which involves a combination of a fishing line and an extension spring. Additionally, flexible footpath floaters on which the fairleads are mounted contribute to the mismatch in the results. When the crest of the wave passes, the footpath

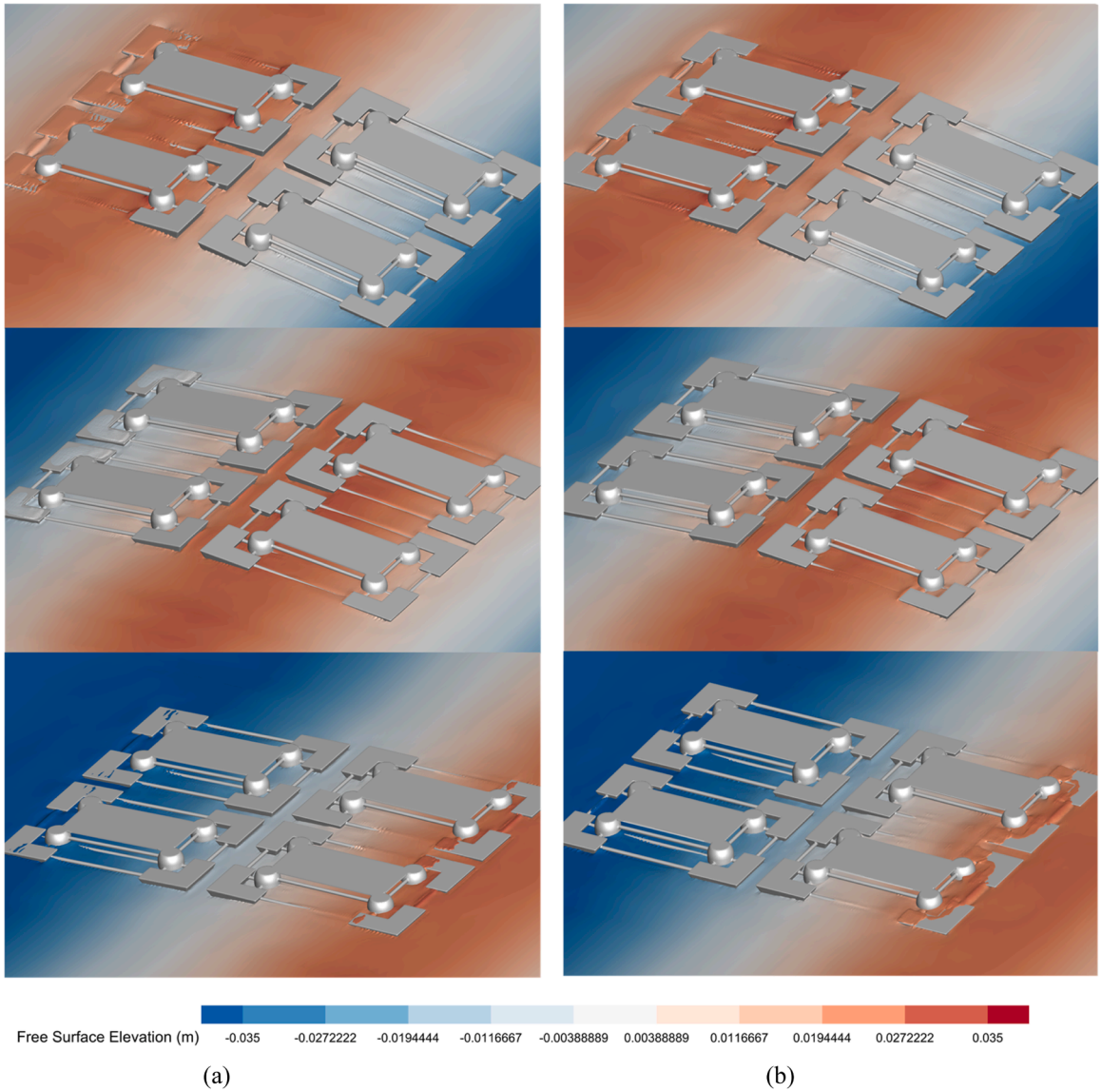

Fig. 16. Wave propagation and overwash patterns through 2×2 FPV array (λ/L = 2.57, H = 7 cm). (a) Spring connector formulation, (b) Rigid Joint formulation.

floaters bend downwards, affecting the fairlead. This motion reduces the extension of the spring, allowing a portion of the load to be shed - an effect that the rigid-body CFD model cannot reproduce.

In Fig. 14(b), the aft mooring line under-predicts the experimental peak tensions by 10–15%, with the most significant discrepancy at $\lambda/L = 4.95$. The underprediction stems from the damping of forces due to frictional components and flexible footpath floaters. Similarly, the trends observed by the CFD model align well with the experimental results. An increase in force is observed with an increase in wave height. At H = 4 cm, an increase in force is observed at $4 < \lambda/L < 6.25$, after which a mild increase is observed. A similar behaviour is observed at H = 5 cm, with a sharp increase noted at $4 < \lambda/L < 6.25$, followed by a mild increase.

4.3. Validation of a 2×2 FPV array

Building on the validated single-module framework, this section examines the hydrodynamic response of the 2×2 FPV array, focusing on inter-row differences arising from wave-field shielding and multi-body coupling. To validate the spring-based connector approach and demonstrate its necessity for rope-mesh FPV systems, this section compares two fundamentally different modelling approaches against experimental measurements: the rigid joint implementation in Section 3.4.1 and the spring connector formulation in Section 3.4.2 . The rigid joint was configured as a joint permitting relative heave and pitch motion while constraining surge and sway, reflecting the dominant motions observed experimentally under head-sea conditions.

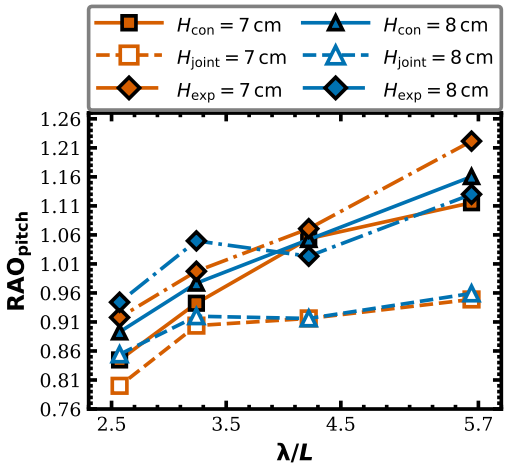

(a) RAO$_{Pitch}$ value for front row at H = 7cm, 8cm

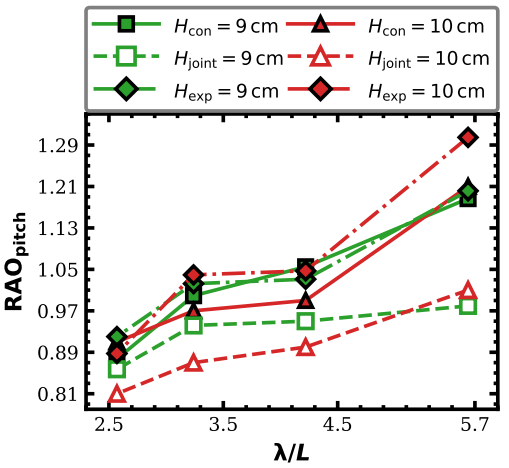

(a) RAO$_{Pitch}$ value for front row at H = 9cm, 10cm

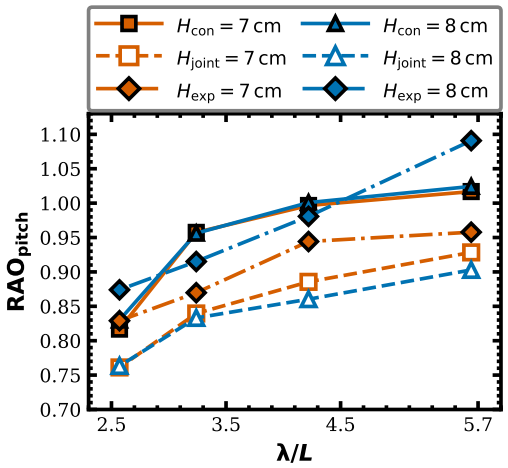

(c) RAO$_{Pitch}$ value for back row at H = 7cm, 8cm

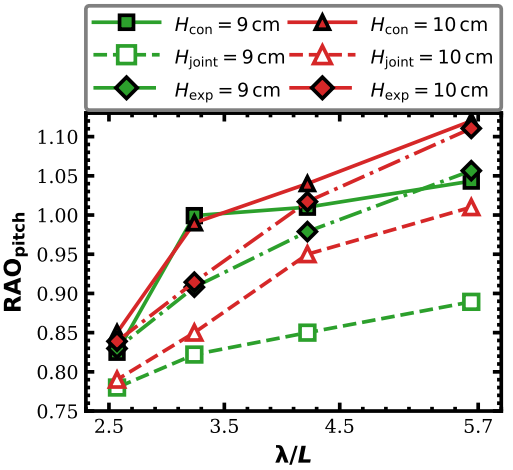

(d) RAO$_{Pitch}$ value for back row at H = 9cm, 10cm

Fig. 17. RAO$_{Pitch}$ value for 2 × 2 array of floaters.

Fig. 15 compares the heave response of the front and back modules of a 2×2 FPV array over $2.5 < \lambda/L < 6$. Four incident wave heights are considered: H = 7 cm, 8 cm, 9 cm, 10 cm. The heave responses obtained using the spring connector and the rigid joint exhibit the same overall wavelength dependence, with RAO$_{heave}$ increasing from λ/L = 2.5 to a local maximum near λ/L ≈ 3–3.5 and then gradually decreasing at longer wavelengths. However, while the trends remain consistent between the two formulations, the rigid joint approach predicts larger response magnitudes, i.e., it overestimates the heave relative to the connector case across most tested conditions. This indicates that the assumed inter-module coupling representation primarily affects the amplitude of the response rather than the qualitative hydrodynamic behaviour.

The spring connector consistently tracks experimental measurements within 5–14% error across all tested conditions, with deviations largest at short wavelengths (λ/L ≈ 2.5–3) where structural flexibility effects become significant. The rigid joint systematically overestimates heave amplitude relative to both the spring connector and experiments, with errors exceeding 20% in most cases. This difference arises from the absence of elastic coupling in heave. The rigid joint permits relative heave motion but provides zero resistance. This lack of resistance eliminates the mechanism present in the physical rope-mesh system, where relative heave motions are resisted by forces in the connecting ropes. Without any resistance to constrain motion, the rigid joint allows excessive heave motion under wave excitation, resulting in overestimated RAO$_{heave}$ values. The spring-based connector, by contrast, applies restoring forces

proportional to the relative displacement, providing the elastic coupling characteristic of rope connections that constrains heave amplitude and dissipates energy through the connection. Overall, the rigid joint overestimates RAO_{heave} by 5–14% relative to the spring connector across all tested conditions, consequently overestimating the experimental results by more than 20%.

The comparison in Fig. 16 demonstrates a fundamental limitation of rigid joint formulations for rope-mesh FPV systems. The connector representation alone produces markedly different overwash predictions, revealing the critical role of mechanical coupling in multi-body FPV dynamics. For the rigid joint configuration, the larger heave limits wave overtopping, resulting in comparatively weaker overwash across the front-row modules. This behaviour is consistent with the overpredicted heave response, as the array undergoes pronounced vertical motion that effectively rides over the incoming waves. In contrast, the spring-connected configuration exhibits substantially increased overwash. The reduced heave response causes the FPV to remain closer to the mean free-surface elevation. Consequently, incident wave crests interact more directly with the FPV surface, generating increased load across the module. The rigid joint's systematic underprediction of overwash indicates that predictions based on rigid joint formulations may not adequately represent operational conditions. Accurate overwash prediction is essential for reliable operational assessment and design of modular FPV arrays.

Quantitatively, the CFD predictions overestimate the experimental heave response. As observed in the single-module validation, this deviation is attributed to physical damping mechanisms present in the experiments but absent in the numerical model. When the incident wavelength is comparable to the characteristic length of the footpath floater, the footpath floaters undergo significant structural flexure, thereby lowering the recorded heave response. Additionally, the presence of the fishing beads between the FPV and shared footpath floaters significantly dampens the overall motion of the FPV, thus contributing to the reduced motion in the experiment. The lack of these damping factors within the CFD model contributes to the overestimated heave values. From the findings, we see two characteristics of this system. For all tested conditions, the heave values show a consistent increase from $\lambda/L=2.5$ to a local maximum near $\lambda/L\approx3$, followed by a gradual decline at longer wavelengths. The observed peak near $\lambda/L\approx3$ corresponds to a region where the incident wavelength becomes comparable to the characteristic length of the platform. At this ratio, the floater experiences near-resonant heave excitation, yielding a temporary amplification of the motion. Beyond this point, as the wavelength increases, the wave steepness decreases, and the free-surface slope flattens, reducing the vertical excitation and consequently the heave amplitude. This behaviour is consistent across all tested wave heights, indicating that the heave motion remains largely linear with respect to wave amplitude.

Comparing the two rows reveals that the aft row heave is systematically lower than the front-row heave across all wavelengths and wave heights. This attenuation, typically within 10%, arises from the wave-field shielding effect induced by the front modules. As incident waves interact with the front row, part of their energy is dissipated through diffraction, radiation, and viscous losses around the module edges. The resulting scattered wave field reaches the rear row with reduced amplitude, leading to weaker excitation and smaller heave responses. The influence of this shielding is least prominent near $\lambda/L\approx3$. Overall, the heave response of the array is governed by wavelength-dependent hydrodynamic coupling and the geometric relationship between platform spacing and wave field. The CFD model successfully captures these trends, validating its suitability for predicting multi-body FPV dynamics and wave–structure interactions.

Fig. 17 depicts the RAO_{Pitch} for the front and back rows across incident wave heights H = 7–10 cm and wavelength ratios $2.5 < \lambda/L < 5.7$. Across all tested conditions, the spring connector consistently predicts higher pitch amplitudes than the rigid joint, with experimental measurements consistently falling closer to the spring connector predictions. The spring connector maintains validation errors within 5–13% of experimental measurements, while the rigid joint exhibits errors of 10–22%. Whether the spring connector slightly overpredicts or underpredicts experiments varies with specific wave conditions, but in all cases, it demonstrates better accuracy compared to the rigid joint, which systematically underpredicts experimental pitch response across all tested conditions.

This difference arises from a fundamental distinction in how the two formulations represent inter-module coupling: the rigid joint permits relative pitch motion but provides zero coupling forces, thereby allowing modules to be kinematically free to rotate without any force transmission between them. In the spring-based connector formulation, the coupling forces create moments, providing an additional pitch contribution to the pitch motion beyond the direct wave-induced motion. The absence of these forces results in a systematic underprediction of pitch response.

The pitch response exhibits a strong and monotonic dependence on wavelength, with larger pitch amplitudes observed at increasing λ/L for both array rows. The front row of floaters shows a steep increase in pitch with increasing wavelength, illustrating how longer wavelengths can promote pitch motion. For H = 7 cm, pitch increases from RAO ≈ 0.86 at $\lambda/L = 2.5$ to RAO ≈ 1.11 at $\lambda/L = 5.7$, representing a 29% increase. At H = 10 cm, the front row pitch increases from RAO ≈ 0.89 to RAO ≈ 1.21, a 36% increase. However, this is the opposite of the response of a single body. The reason for this behaviour can be attributed to the multibody interaction. The back row of floaters is influenced by diffraction and radiated waves that arrive out of phase with the incident waves. At short wavelengths, the two rows attempt to pitch out of phase with each other. The presence of connections between floaters resists this differential motion, constraining pitch amplitude. As the wavelength increases, the phase difference diminishes, and inter-row coupling becomes less constraining, allowing the FPVs to rotate more freely. This contributes to the increased pitch response as the wavelength increases. Across all tested conditions, the CFD results reproduce the general trend of the experiments but consistently predict the pitch value within 13%. This arises primarily from the rigid-body assumption in the numerical model, which neglects the elastic response of the connecting footpath floaters and the local flexibility of the polyamide structure. In the experiments, flexible elements permit small additional rotations, especially under high wave steepness, leading to slightly higher measured RAO values.

Comparing front and back rows reveals that the back row exhibits systematically lower pitch response across all wavelengths and wave heights. At H = 7 cm and $\lambda/L = 5.7$, back row pitch reaches RAO ≈ 1.03 compared to RAO ≈ 1.11 for the front row using the spring connector—a 7% reduction. At H = 10 cm and the same wavelength, back row pitch reaches RAO ≈ 1.05 versus RAO ≈ 1.21 for

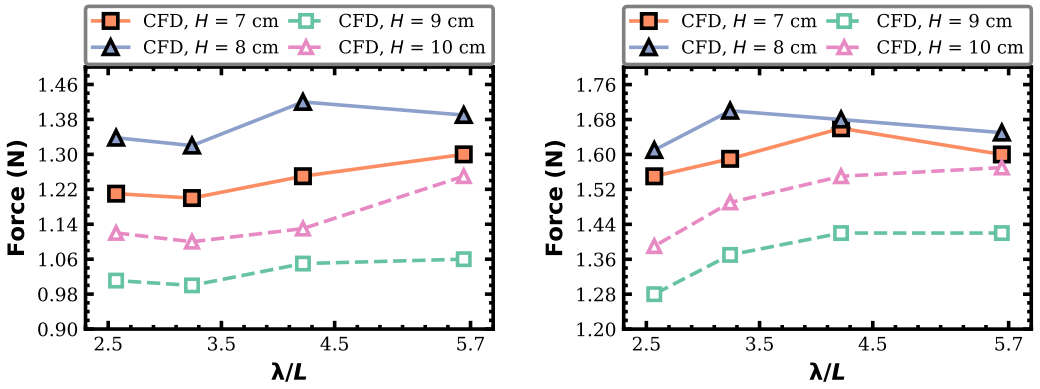

(a) Mooring force for front row of FPV array

(b) Mooring force for back row of FPV array

Fig. 18. Mooring forces for the FPV array.

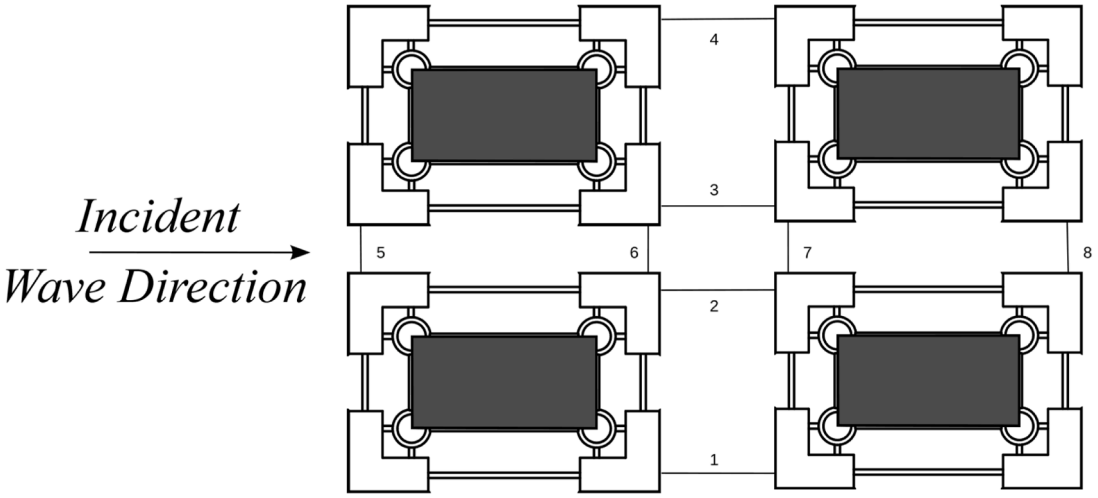

Fig. 19. Schematic of connector arrangement for the 2×2 FPV array (top view). Connectors 1–4 provide streamwise coupling between front and rear rows; connectors 5–8 provide transverse coupling within each row.

the front row—a 13% reduction. Across all tested conditions, this back row attenuation ranges from 8–13%, arising from two mechanisms. First, wave-field shielding by the front modules reduces excitation amplitude reaching the back row. As incident waves interact with the front row, energy is dissipated through diffraction, radiation, and viscous losses, resulting in a scattered wave field with reduced amplitude reaching the rear modules. Second, inter-row coupling through connectors resists differential rotation between front and back rows. When the front row pitches in response to incident waves, the connecting ropes generate forces that oppose relative rotation, hindering the pitch motion of the back row. Both mechanisms contribute to the observed 8–13% reduction in back row pitch response.

Fig. 18(a) and (b) quantify the mooring force for the front and aft FPV units against non-dimensional wavelength, at four wave heights H = 7 cm, 8 cm, 9 cm, and 10 cm, respectively. Two characteristics are observed: First, the mooring force increases as the wave height increases. Secondly, wavelength exhibits three regimes (i) A slight increase (or) a plateau at $\lambda/L < 3$. This is followed by a steep load increase at $3 < \lambda/L < 5$, followed by a mild increase or a plateau. In Fig. 18a, the force increases monotonically with incident wave height. At H = 7 cm, front row tension rises from 1 N at $\lambda/L = 2.7$ to 1.1 N at $\lambda/L = 5.8$, and for H = 10 cm, it rises from 1.3 N at $\lambda/L = 2.7$ to 1.5 N at $\lambda/L = 5.8$. At $\lambda/L < 3$, the mooring values are nearly constant. At $3 < \lambda/L < 5$, there is a sharp rise in the mooring force, increasing the force by 8–12%. At $\lambda/L > 2.7$, in Fig. 18b, a similar behaviour is observed. Unlike Fig. 17a, at $2.6 < \lambda < 3.5$, there is a progressive increase in the mooring force. At H = 7 cm, front row tension rises from 1.25 N at $\lambda/L = 2.7$ to 4.5 N at $\lambda/L = 5.8$, and for H = 10 cm, it rises from 1.45 N at $\lambda/L = 2.7$ to 1.75 N at $\lambda/L = 5.8$.

Throughout the study on mooring forces, we have identified that the aft mooring force is always greater than the forward mooring

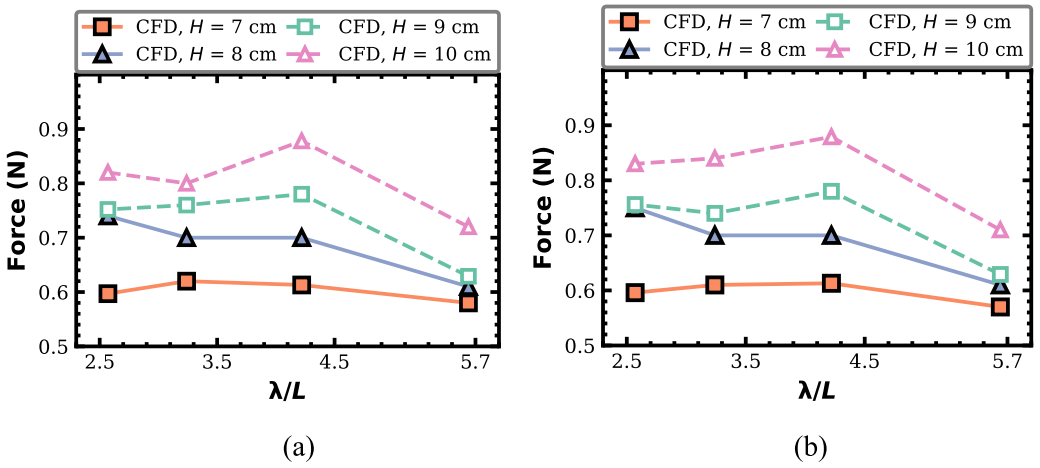

Fig. 20. Peak streamwise connector forces (Fmax) as a function of non-dimensional wavelength for the 2×2 FPV array (a) Connector 1 (b) Connector 3.

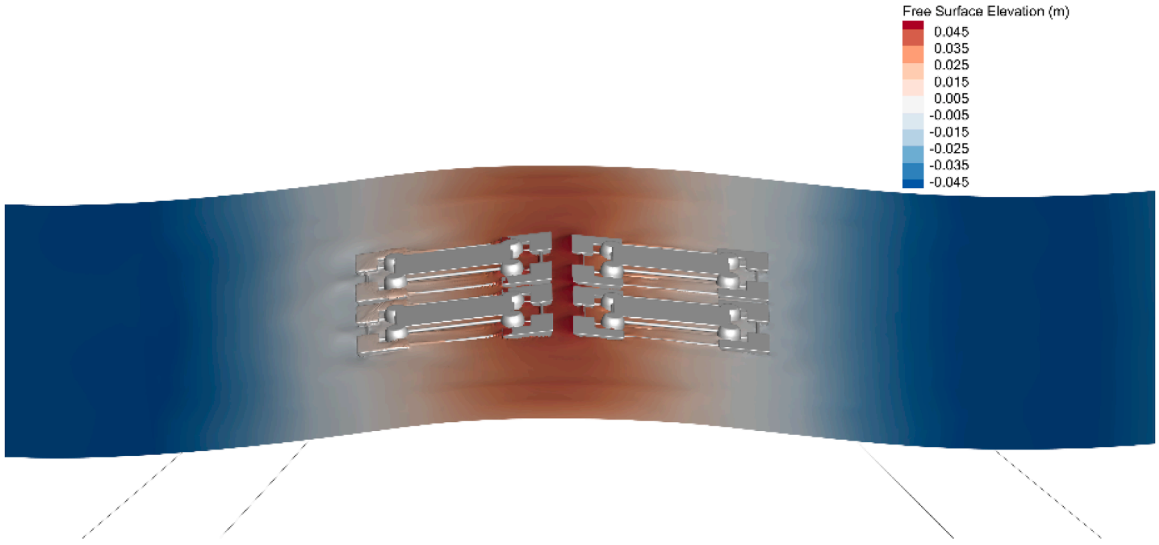

Fig. 21. Free-surface profile and FPV array configuration at wave crest passage for short-wave condition (λ/L = 2.5, H = 0.09 m), showing rapid variation in wave elevation across the array length with front and rear rows experiencing different wave elevations simultaneously.

force. This is true for both a single array and a 2×2 array. The primary reason for this is second-order drift. Second-order drift arises from non-linear effects, such as the interaction between wave diffraction, radiation, and incident waves [37]. Unlike first-order forces, which are linear and oscillatory, second-order forces result in low-frequency motions, such as surge and pitch, in floating structures [37]. This interaction, when averaged over multiple wave cycles, results in a net force that gently pushes the floater forward, increasing the extension on the aft mooring and thereby increasing the mooring force. The amplification of the aft mooring is observed by [38,39]. Consequently, the forward lines become slacker, decreasing their tension. The validation against experimental data demonstrates that the spring-based connector formulation accurately reproduces the hydrodynamic response of the rope-mesh FPV array.

4.4. Analysis of connection force

With the spring-based connector approach validated, we now examine the connector forces themselves. Understanding these forces is critical for structural design, fatigue analysis, and material selection for rope-mesh FPV systems. This section characterises how connector loads vary with wavelength, wave height, and position within the array.

Fig. 19 illustrates the connector arrangement employed in the 2×2 FPV array. Eight connectors link the four FPV modules: connectors 1–4 provide longitudinal (streamwise) coupling between the front and rear rows, while connectors 5–8 provide transverse

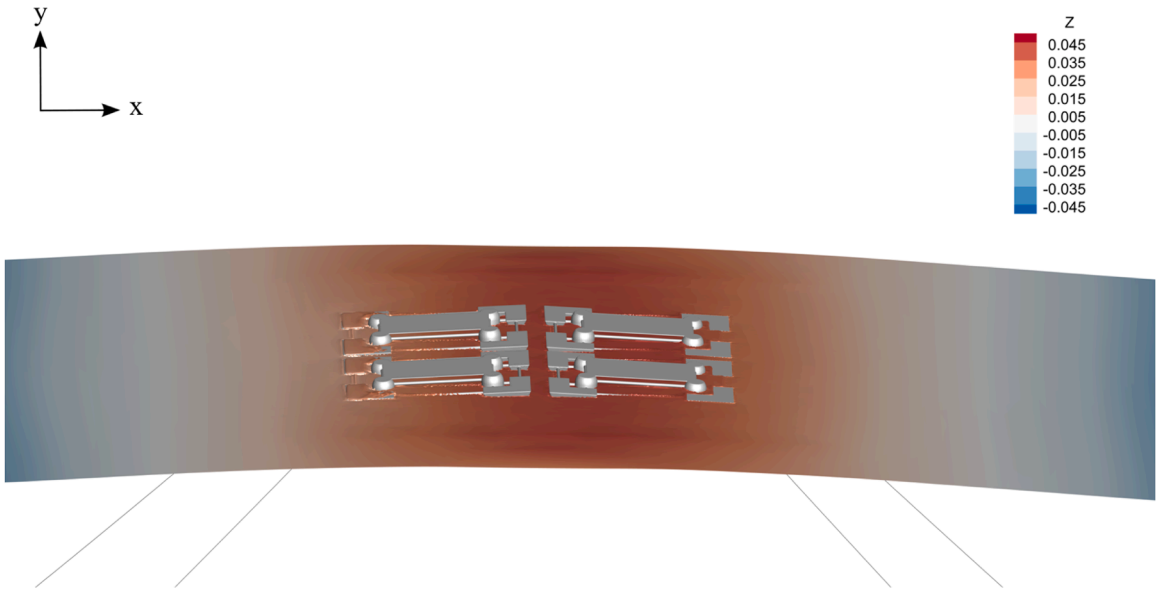

Fig. 22. Free-surface profile and FPV array configuration at wave crest passage for long-wave condition ($\lambda/L = 5.7$, $H = 0.09$ m), showing gradual variation in wave elevation across the array, with both rows experiencing similar wave phases.

coupling between the left and right modules within each row.

Fig. 20 summarises the connector force response as a function of non-dimensional wavelength (λ/L) for four incident wave heights, distinguishing between connectors aligned with the direction of wave propagation (Connectors 1 and 3, streamwise coupling between the front and back modules). The connector forces presented in this section represent the maximum tension recorded over the final five wave periods after the simulation reached periodic steady state. For each connector, the instantaneous force F(t) was monitored throughout the simulation, and the peak value over the last five cycles was extracted for analysis. This peak force metric is appropriate for structural design and fatigue assessment, as it captures the maximum load demand experienced by each connector under each wave condition.

The wavelength dependence of streamwise connector forces (Connectors 1 and 3) is governed by the magnitude of relative motion between front and rear rows. As incident waves propagate through the array, differential surge, heave, and pitch responses cause time-varying extension of the connecting elements. The peak connector tension at each wavelength varies with the maximum relative displacement between attachment points, which depends on the phase relationship between front-row and rear-row motions.

This mechanism is illustrated by comparing free-surface profiles at wave crest passage for a short-wave and long-wave condition at the same incident height. In the short-wave case ($\lambda/L = 2.5$, Fig. 21), the free surface varies rapidly over the array length, causing the front and rear rows to encounter different phases of the wave simultaneously; when one row experiences the wave crest, the other may be positioned near the trough. This phase difference causes the two rows to move out of phase, producing maximum connector extension and therefore peak tension.

In contrast, the long-wave condition ($\lambda/L = 5.7$, Fig. 22) exhibits a much more gradual free-surface profile that remains nearly uniform across the array. At this wavelength, the array dimensions are small relative to the wavelength, such that both rows experience similar wave phase and pressure gradient. The phase difference between incident and scattered waves diminishes, and the two rows therefore respond more synchronously. This coherent motion minimises relative displacement between attachment points, reducing connector extension and therefore the force.

When the incident wavelength is comparable to the array's streamwise dimension ($\lambda/L \approx 2$–4), the variation of the wave steepness causes front and rear rows to experience different wave phases, inducing strong differential motion and maximising connector loading. As wavelength increases beyond this critical range, the wave becomes more uniform across the array, and both rows respond more synchronously, reducing relative displacement and therefore connector demand.

Fig. 23 depicts the peak forces on the transverse connector. In contrast to streamwise connectors, transverse connectors exhibit much lower force magnitudes and weaker wavelength dependence. Forces remain below 0.3 N even at the highest wave height. Under head-sea conditions, modules connected by transverse connectors experience nearly simultaneous wave forcing, resulting in minimal differential motion in the transverse direction. The weak wavelength dependence confirms that transverse loading is not primarily driven by wave-induced differential motion between left-right module pairs.

Examination of the individual transverse connectors reveals that Connector 5 experiences forces 30–40% higher than Connector 6 (front-right transverse) under comparable conditions. Similarly, Connector 8 (rear-right) carries moderately higher forces than Connector 7 (rear-left). This pattern arises from mooring-induced effects: mooring lines attached at the array corners pull outward, extending transverse connectors near these attachment points and generating higher elastic forces. Connectors 5 and 8, positioned near the front-left and rear-right corners respectively, experience greater extension than the more inboard Connectors 6 and 7. Connector 5

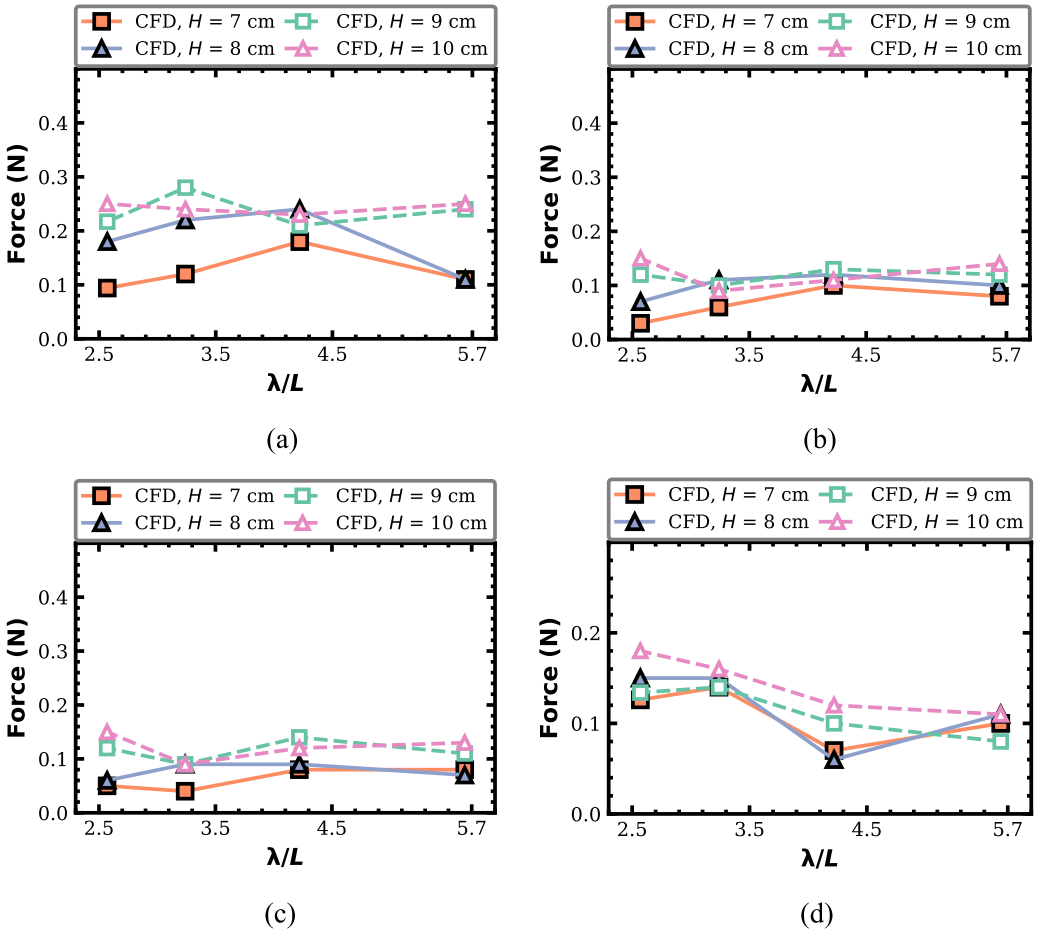

Fig. 23. Peak transverse connector forces (Fmax) as a function of non-dimensional wavelength for the 2×2 FPV array (a) Connector 5 (b) Connector 6 (c) Connector 7 (d) Connector 8.

exhibits the highest forces overall, as it is subjected to both direct wave excitation at the upstream position and mooring-induced extension. Connector 8 experiences moderately elevated forces despite partial wave sheltering in the rear row, while Connectors 6 and 7, positioned away from mooring corners, carry the lowest transverse loads.

The observed force distribution has important implications for rope-mesh FPV array design. Streamwise connectors constitute the critical design drivers under head-sea loading, with peak forces occurring at $\lambda/L \approx 2.5$–3.5, where phase-lag effects maximise differential motion between rows. Design wave conditions should consider not only extreme wave heights but also wavelength distributions characteristic of the deployment site, as long-period swell generates substantially lower connector loads than short- to intermediate-period waves. Among transverse connectors, those positioned near mooring attachment points require higher design margins to account for combined wave and mooring loading, while inboard connectors may be designed with lower safety factors.

5. Conclusions

This study developed and validated a high-fidelity CFD framework for simulating the coupled hydrodynamic response of rope-mesh FPV arrays under regular wave conditions. The framework integrates OpenFOAM's interFoam solver with MoorDyn mooring dynamics and implements an in-memory spring connector formulation within the rigidBodyMotion framework to represent tensioned rope connections between modules. This force-based approach addresses the limitations of conventional joints, which cannot capture the stiffness and moment-generating characteristics of tensioned rope connections.

Validation against wave tank experiments for both single-module and 2×2 array configurations demonstrated excellent predictive accuracy. For the single module, heave and pitch RAOs were reproduced within 10% across wavelengths from $\lambda/L = 4$ to 11. For the 2×2 array, validation errors remained within 5–14% for heave and 8–13%. The framework successfully captured multi-body interaction effects, including wave-field shielding that reduces aft-row response within 10% relative to the front row.

Direct comparison with a rigid joint confirmed the necessity of the spring-based approach for tensioned rope systems. This work reproduces experimental motion responses within 5–13%, while a publicly available counterpart approach exhibits errors exceeding

20% for heave and pitch at long wavelengths. This improvement arises from the spring connector's ability to generate configuration-dependent moments through force-based compliance, which rigid kinematic joints cannot represent. The spring connector formulation is essential for accurate hydrodynamic prediction of rope-connected FPV arrays.

Connector force analysis revealed strongly anisotropic loading under head-sea conditions. Streamwise connectors experience peak forces at $\lambda/L \approx 2.5–3.5$, where variation in wave elevation creates phase differences between front and rear rows. Transverse connectors experience forces 3–5 times smaller due to symmetric waves on left-right module pairs, with left and right modules moving nearly in unison. Connector forces scale linearly with wave amplitude across all tested conditions. For design purposes, streamwise rope connections constitute the critical load path and should govern rope sizing, connection strength, and fatigue life calculations for rope-mesh FPV systems under head-sea loading.

The validated CFD framework, together with the novel spring-based connector formulation, provides a robust foundation for preliminary design studies of modular FPV systems. Future work should extend the methodology to investigate larger array configurations to establish scaling relationships. Such extensions will provide practical design guidance for the emerging generation of nearshore and offshore FPV installations.

CRediT authorship contribution statement

Aditya Nair: Writing – original draft, Visualization, Validation, Software, Investigation. **Chenhao Mi:** Validation, Software. **Patrick G Verdin:** Formal analysis, Writing – review & editing, Validation, Supervision. **Luofeng Huang:** Writing – review & editing, Supervision, Project administration, Funding acquisition, Conceptualization.

Declaration of competing interest

The authors declare that they have no known competing financial interests or personal relationships that could have appeared to influence the work reported in this paper.

Data availability

All data underlying the results are available as part of the article andno additional source data is required.

References

[1] Cipriani G, Di Dio V, Dioguardi A, Guarino S. Comparative analysis of the performance of floating and ground-mounted photovoltaic panels: an experimental approach. In: Proceedings - 24th EEEIC International Conference on Environment and Electrical Engineering and 8th I and CPS Industrial and Commercial Power Systems Europe, EEEIC/I and CPS Europe 2024. Institute of Electrical and Electronics Engineers Inc.; 2024. https://doi.org/10.1109/EEEIC/ICPSEurope61470.2024.10751096.
[2] Attar H, Alahmer A, Borowski G, Alsaqoor S. Comprehensive review of advancements, challenges, design, and environmental impact in floating photovoltaic systems. Ecol Eng Environ Technol 2025;26:301–22. https://doi.org/10.12912/27197050/199520.
[3] Song J, Imani H, Yue J, Yang S. Hydrodynamic characteristics of floating photovoltaic systems under ocean loads. J Mar Sci Eng 2023;11:1813.
[4] Panjwani B. Assessment of breakwater as a protection system against aerodynamic loads acting on the floating PV system. Energies (Basel) 2024;17:4873.
[5] Yan C, Shi W, Han X, Li X, Verma AS. Assessing the dynamic behavior of multiconnected offshore floating photovoltaic systems under combined wave-wind loads: A comprehensive numerical analysis. Sustain Horizons 2023;8. https://doi.org/10.1016/j.horiz.2023.100072.
[6] Al-Yacouby AM, Halim ERBA, Liew MS. Hydrodynamic analysis of floating offshore solar farms subjected to regular waves. Lecture notes in mechanical engineering. Singapore: Springer Singapore; 2020. p. 375–90.
[7] Baruah G, Karimirad M, Friel D, Mackinnon P, Abbasnia A, Sarmah N. Development of a CFD model for simulating a floating solar platform in irregular wave regimes. Trends in renewable energies offshore. London: CRC Press; 2022. p. 717–25.
[8] Dhaifullah MH, Jifaturrohman MI, Putranto T, Setyawan D, Utama IKAP, Huang L. Enhancing pure oscillatory response motion performance: innovative designs for semi-submersible and catamaran floating photovoltaic systems (FPVs) in various sea-State conditions. In: Proceedings of the 2024 International Conference on Sustainable Energy: Energy Transition and Net-Zero Climate Future, ICUE 2024. Institute of Electrical and Electronics Engineers Inc.; 2024. https://doi.org/10.1109/ICUE63019.2024.10795525.
[9] Wei Y, Ou B, Wang J, Yang L, Luo Z, Jain S, Hetharia W, Riyadi S, Utama I, Huang L. Simulation of a floating solar farm in waves with a novel sun-tracking system. IOP Conf Ser Mater Sci Eng 2023;1288:012041.
[10] Sui S, Cao L, Gao Y, Huo Z, Chen Q. Numerical simulation study on hydrodynamic characteristics of offshore floating photovoltaics. J Mar Sci Eng 2025;13:142.
[11] Wei Y, Zou D, Zhang D, Zhang C, Ou B, Riyadi S, Utama IKAP, Hetharia W, Wood T, Huang L. Motion characteristics of a modularized floating solar farm in waves. Phy Fluids 2024;36. https://doi.org/10.1063/5.0199248.
[12] Jifaturrohman MI, Utama IKAP, Putranto T, Setyawan D, Huang L. A study into the correlation between single array-hull configurations and wave spectrum for floating solar photovoltaic systems. Ocean Eng 2024;312:119312.
[13] Xu W, Sun Y, He Z. Hydrodynamic performance study of floating photovoltaic arrays with multiple floating bodies. Appl Ocean Res 2024;153:104286.
[14] Wang B, Li Y, Huang L, Yao Y, Qin Y. Dynamic analysis of a novel star-type floating photovoltaic system with flexible connectors. Ocean Eng 2024;304:117854. https://doi.org/10.1016/j.oceaneng.2024.117854.
[15] Zou T, Jiang J, Li H, Du J, Tao L. Structural responses of offshore multi-body floating photovoltaic array under different connection conditions. Appl Ocean Res 2025;158. https://doi.org/10.1016/j.apor.2025.104544.
[16] Ma G, Zhang C, Chen H, Hou W, Wang W, Zhang J. Hydrodynamic analysis of floating photovoltaic system constrained with rigid connectors. Sci Rep 2024;14:29920. https://doi.org/10.1038/s41598-024-81245-w.
[17] Wang B, Li Y, Huang L, Yao Y, Qin Y. Dynamic analysis of a novel star-type floating photovoltaic system with flexible connectors. Ocean Eng 2024;304. https://doi.org/10.1016/j.oceaneng.2024.117854.
[18] Ji C, Gao X, Xu S. Study on the influence of connector designs on the hydrodynamic performance of an offshore floating photovoltaic. Ocean Eng 2024;308. https://doi.org/10.1016/j.oceaneng.2024.118298.
[19] Yao Y, Zhang X, Deng Z, Ren X, Song J, Yang X. Hydrodynamic analysis of offshore floating photovoltaic structure with elastic connection. Mar Energy Res 2025;2:10011. https://doi.org/10.70322/mer.2025.10011. –10011.

[20] Zhang G, Bao F, Jiang C, el Moctar O, Xu Z, Zhou B. Hydrodynamic performance of floating solar arrays with articulated modules for optimal wave adaptation. Appl Ocean Res 2025;164. https://doi.org/10.1016/j.apor.2025.104762.
[21] Yan C, Shi W, Han X, Li X, Verma AS. Assessing the dynamic behavior of multiconnected offshore floating photovoltaic systems under combined wave-wind loads: A comprehensive numerical analysis. Sustain Horizons 2023;8. https://doi.org/10.1016/j.horiz.2023.100072.
[22] Leventopoulou T, Dai J, Jiang Z. Hydroelastic analysis of interconnected offshore floating photovoltaic floats. J Offshore Mech Arct Eng 2025;147. https://doi.org/10.1115/1.4068495.
[23] Ma G, Zhang C, Chen H, Hou W, Wang W, Zhang J. Hydrodynamic analysis of floating photovoltaic system constrained with rigid connectors. Sci Rep 2024;14. https://doi.org/10.1038/s41598-024-81245-w.
[24] Lee JH, Paik KJ, Lee SH, Hwangbo J, Ha TH. Experimental and numerical study on the characteristics of motion and load for a floating solar power farm under regular waves. J Mar Sci Eng 2022;10. https://doi.org/10.3390/jmse10050565.
[25] Mi C, Verdin PG, Nair A, Lyu X, Yang Y, Sherif A, Silva D, Huang L. An experimental study on the hydrodynamic performance of modular rope mesh floating solar platforms. Ocean Eng 2025;339. https://doi.org/10.1016/j.oceaneng.2025.122175.
[26] Jacobsen NG, Fuhrman DR, Fredsøe J. A wave generation toolbox for the open-source CFD library: OpenFoam®. Int J Numer Methods Fluids 2012;70:1073–88. https://doi.org/10.1002/fld.2726.
[27] Chen H, Hall M. CFD simulation of floating body motion with mooring dynamics: coupling MoorDyn with OpenFOAM. Appl Ocean Res 2022;124. https://doi.org/10.1016/j.apor.2022.103210.
[28] Chen H, Medina TA, Cercos-Pita JL. CFD simulation of multiple moored floating structures using OpenFOAM: an open-access mooring restraints library. Ocean Eng 2024;303:117697. https://doi.org/10.1016/j.oceaneng.2024.117697.
[29] Hall M, Goupee A. Validation of a lumped-mass mooring line model with DeepCwind semisubmersible model test data. Ocean Eng 2015;104:590–603. https://doi.org/10.1016/j.oceaneng.2015.05.035.
[30] C.W. Hirt, B.D. Nichols, Volume of fluid (VOF) method for the dynamics of free boundaries*, 1981.
[31] M. Wu, CFD with OpenSource software - coupled motion of two floating objects, 2016. https://www.tfd.chalmers.se/~hani/kurser/OS_CFD_2015/MinghaoWu/FinalReport_Minghao_Wu.pdf (accessed March 27, 2024).
[32] Larsen BE, Fuhrman DR, Roenby J. Performance of interFoam on the simulation of progressive waves. Coastal Eng J 2019;61:380–400. https://doi.org/10.1080/21664250.2019.1609713.
[33] Windt C, Davidson J, Schmitt P, Ringwood JV. On the assessment of numerical wave makers in CFD simulations. J Mar Sci Eng 2019;7:47. https://doi.org/10.3390/jmse7020047.
[34] Connell KO, Cashman A. Development of a numerical wave tank with reduced discretization error. In: International Conference on Electrical, Electronics, and Optimization Techniques, ICEEOT 2016. Institute of Electrical and Electronics Engineers Inc.; 2016. p. 3008–12. https://doi.org/10.1109/ICEEOT.2016.7755252.
[35] Karola A, Tavakoli S, Mikkola T, Matusiak J, Hirdaris S. The influence of wave modelling on the motions of floating bodies. Ocean Eng 2024;306. https://doi.org/10.1016/j.oceaneng.2024.118067.
[36] Hu ZZ, Greaves D, Raby A. Numerical wave tank study of extreme waves and wave-structure interaction using OpenFoam®. Ocean Eng 2016;126:329–42. https://doi.org/10.1016/j.oceaneng.2016.09.017.
[37] Zhang Z, Guan L, Wu H, Wu L, Liu W, Cui L. Effects of the second-order hydrodynamics on the dynamic behavior of the platform among the wind-wave hybrid systems. J Eng Res (Kuwait) 2025;13:1603–16. https://doi.org/10.1016/j.jer.2024.04.003.
[38] Ji C, Gao X, Xu S. Study on the influence of connector designs on the hydrodynamic performance of an offshore floating photovoltaic. Ocean Eng 2024;308. https://doi.org/10.1016/j.oceaneng.2024.118298.
[39] Mei X, Xiong M. Effects of second-order hydrodynamics on the dynamic responses and fatigue damage of a 15 mw floating offshore wind turbine. J Mar Sci Eng 2021;9. https://doi.org/10.3390/jmse9111232.

https://dspace.org/

High-fidelity simulation of a novel rope-mesh structure for a floating photovoltaic array in waves

Nair, Aditya; Mi, Chenhao; Verdin, Patrick G.; Huang, Luofeng

2026-07-15
Elsevier
https://doi.org/10.1016/j.marstruc.2026.104089
Nair A, Mi C, Verdin PG, Huang L. (2026) High-fidelity simulation of a novel rope-mesh structure for a floating photovoltaic array in waves. Marine Structures, Volume 109, July 2026, Article number 104089

Downloaded from a DSpace repository. https://dspace.org/